Supporting Information for

Bimetallic Effect of Single Nanocatalysts Visualized by Super-Resolution Catalysis Imaging

Guanqun Chen,[a] Ningmu Zou,[a] Bo Chen,[a] Justin B. Sambur,[a,b] Eric Choudhary,[a,c] Peng Chen[a,*]

[a] Department of Chemistry and Chemical Biology, Cornell University, Ithaca, New York 14853, U.S.A.

[b] Present address: Department of Chemistry, Colorado State University, Fort Collins, Colorado 80523, U.S.A.

[c] Present address: Building 201, B-S-05, 3M Center, St. Paul, Minnesota 55144, U.S.A.

 * Correspondence to: pc252@cornell.edu

Contents

1. General instruments and experiment methods

Resazurin used in the single-molecule catalysis imaging experiment was from Molecular Probes (99%, Cat no. R12204) with further purification by thin layer chromatography (TLC). Resazurin used in ensemble activity test was without TLC purification. Resorufin was from Sigma-Aldrich (95%; Cat no. 424455). All other chemicals were purchased from Sigma-Aldrich and used as received unless specified otherwise. All experiments were done at room temperature under ambient conditions unless specified otherwise. General instruments are listed here: UV-Vis spectra were measured on a Beckman Coulter DU800 spectrophotometer. Fluorescence spectra were measured on an Agilent Eclipse fluorometer. TEM (FEI Tecnai T12), high-resolution TEM (HRTEM, FEI Tecnai F20), SEM (LEO 1550) and related sample preparation were performed at the Cornell Center for Materials Research (CCMR) and the Cornell NanoScale Facility (CNF). The super-resolution reaction imaging experiment was carried out on a home-built prism-type wide-field total internal reflection fluorescence microscope. Image analyses were done using home-written MATLAB codes. FDTD simulations were performed using the Lumerical Solutions package. DFT calculations were performed using the Vienna Ab initio Simulation Package (VASP) and Gaussian 09 software.

All other instruments will be specifically described in the following sections.

2. Synthesis and characterizations of mesoporous-silica-coated PdAu nanoparticles

2.1 PdAu nanoparticles

PdAu nanoparticles were prepared via hydrothermal synthesis following Huang et al[1]. 17.7 mg $PdCl_2$, 300 mg NaI and 800 mg polyvinylpyrrolidone (PVP, MW = 55000) were dissolved in 18 mL nanopure water. Under stirring, the mixture was heated to 60 °C for 1 h in order to get a homogeneous solution and then transferred into a 100 mL Teflon-lined autoclave. The reactor was kept at 200 °C for 16 h to grow Pd nanorods (Figure S1A). Without purification, the resulting solution containing Pd nanorods (cooled down to room temperature) was directly used to make PdAu nanoparticles, in which the Au particle was grown at the ends of Pd nanorods. 6 mL of the as-synthesized Pd nanorod solution was mixed with 10 μL 0.15 M $HAuCl_4$ aqueous solution. The mixture was heated at 80 °C under vigorous stirring for 1 h to form PdAu bimetallic nanoparticles via galvanic replacement of Pd by Au. The final solution containing PdAu nanoparticles was mixed with isopropanol and centrifuged at 10,000 g for 10 min to remove the supernatant. The wash with isopropanol and precipitation were repeated once more for better purification. The precipitated PdAu nanoparticles were re-dispersed in 10 mL water for later silica shell coating. According to Huang et al[1], these Pd nanorods are likely 5-fold twinned structure with five {100} side surfaces along the ⟨110⟩ direction.
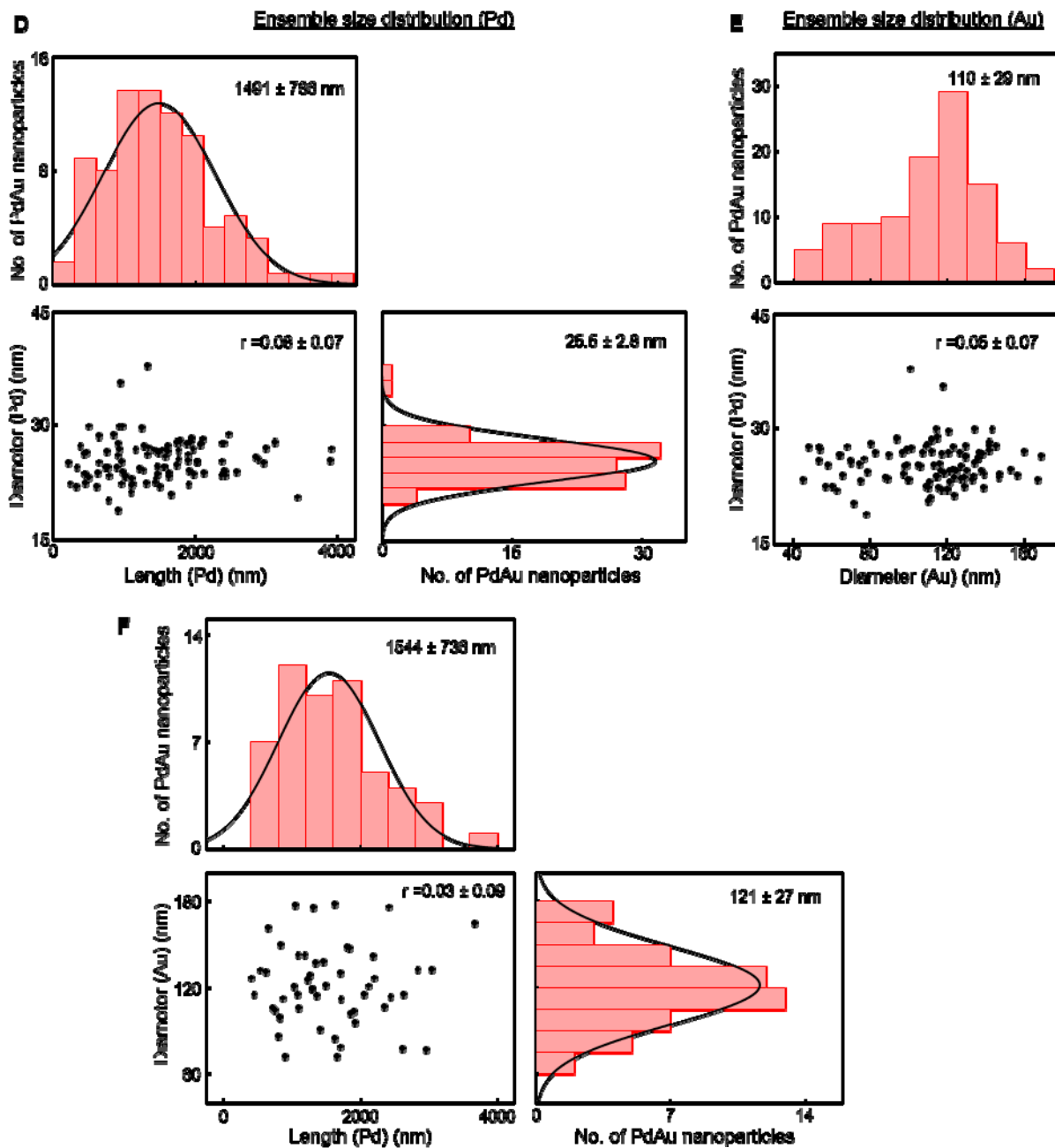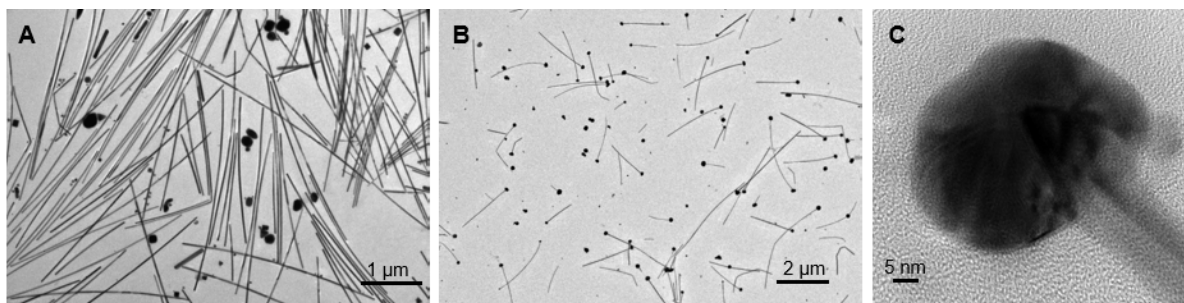
2

Figure S1. Structure characterizations of PdAu nanoparticles. (**A-B**) TEM images of Pd nanorods (A) and PdAu nanoparticles (B). (**C**) HRTEM image of an exemplary PdAu nanoparticle. It shows that the end of Pd nanorod was

buried in the Au nanoparticle. (**D**) Size measurement of the Pd nanorod part of individual PdAu nanoparticles. Upper and right: distributions of the Pd nanorod length and diameter, respectively. Lower left: correlation between the diameter and length of 104 individual Pd nanorods. (**E**) Size measurement of the Au nanoparticle part of 104 individual PdAu nanoparticles: distribution of the Au nanoparticle diameter (upper) and the correlation plot of the Au nanoparticle diameter and Pd nanorod diameter (lower). (**F**) Size measurement of 53 PdAu nanoparticles used in the super-resolution catalysis imaging study. Upper and right: distributions of the Pd nanorod length and Au nanoparticle diameter, respectively. Lower left: correlation between the Au nanoparticle diameter and Pd nanorod length.

From the TEM image of PdAu nanoparticles (Figure S1B), the Au nanoparticles predominantly grow only on one end of the Pd nanorod, but occasionally could be on both ends. The length of the Pd nanorod part varied from several hundred nanometers to microns with an average of ~1500 nm, while the Pd nanorod diameter was mono-dispersed, ~25.5 ± 2.8 nm (Figure S1D). The Au nanoparticle diameter was about 110 ± 29 nm (Figure S1E, upper). There is no correlation between the length and the diameter of Pd nanorod (Figure S1D, lower left), or between the diameter of Au nanoparticle and that of Pd nanorod (Figure S1E, lower). HRTEM of the PdAu nanoparticles (Figure S1C) shows that the original end of the Pd was embedded in the Au nanoparticle, suggesting that the exposed bimetallic interface is on the side-facets of the Pd nanorods.

2.2 PdAu nanoparticle encapsulation by mesoporous silica shell

The PdAu nanoparticles were coated by a mesoporous silica shell using a procedure slightly modified from what we reported previously[2-4]. There were three steps involved: shell growth, shell etching, and sample activation:

(1) Shell growth: 100 μL 0.11 M 3-mercaptopropionic acid (MPA) in ethanol (instead of MPTMS in previous references[2-4]) was added to 10 mL PdAu nanoparticle aqueous solution under stirring for a 24 h ligand exchange. Then 100 μL 17 mM sodium silicate (Fisher Scientific) solution was added into the nanoparticle solution for an initial thin-layer-silica growth on PdAu nanoparticles. The resulting solution (pH adjusted to 9 by 2 M HCl) was stirred for 48 h and then centrifuged at 3,000 g to remove the supernatant. The precipitate was re-dispersed in a 10 mL 4:1 v/v ethanol/water mixture for further shell growth. 120 μL 10% (v/v) tetraethyl orthosilicate (TEOS) in ethanol and 100 μL 0.1 M NaOH solution were added into the mixture under vigorous stirring to grow a thicker silica shell. After 24 h growth, the solution was centrifuged at 3,000 g and the precipitate containing silica-coated PdAu nanoparticles (Figure S2A, C) was collected. The silica shell thickness was ~125 nm (Figure S2E, upper). The coated PdAu nanoparticles were re-dispersed in 12 mL 11:1 v/v water/ethanol mixture to etch the shell to be mesoporous.

(2) Shell etching: The above silica-coated PdAu nanoparticle solution was mixed with 60 μL 0.1 M cetyltrimethylammonium bromide (CTAB) and 60 μL 0.1 M NaOH solutions. The mixture was stirred for 30 min and then heated at 90 °C for 40 min to etch the silica shell. The resulting solution was cooled to room temperature and centrifuged at 3,000 g to collect mesoporous-silica-coated PdAu nanoparticles as precipitate. The final sample was washed by water and ethanol multiple times and dried in air. According to a previous study[4], the formed mesoporous silica shell has ordered wormhole-like pores. The average pore size is ~35 Å; and its specific surface area is ~1000 $m^2\,g^{-1}$.

(3) Sample activation: The organic compounds (i.e. PVP and CTAB) introduced in the earlier synthesis were removed via UV/ozone treatment, in which the dried sample was placed 2-3 cm away from a UV lamp (Ultraviolet, GPH357T5VH/4) and treated overnight. After UV/ozone treatment, the sample was re-dispersed in 1 mL water. An adequate amount (~10 μL) of 0.1 M $NaBH_4$ solution was added into the solution until the color was changed from brown to gray and kept for 5 min. (Note: too long an

incubation in this solution would lead to a complete etching away of the shell, as NaBH$_4$ solution is basic.) The color change indicated that palladium oxide formed during the UV/ozone treatment was reduced to Pd[5]. Finally, the sample was washed by water (and then centrifuged down at 5,000 g to remove supernatant) multiple times to remove the unreacted NaBH$_4$. The final mesoporous silica shell thickness is ~114 nm (Figure S2E, lower), and the PdAu nanoparticle cores maintain their morphology (Figure S2B, D).
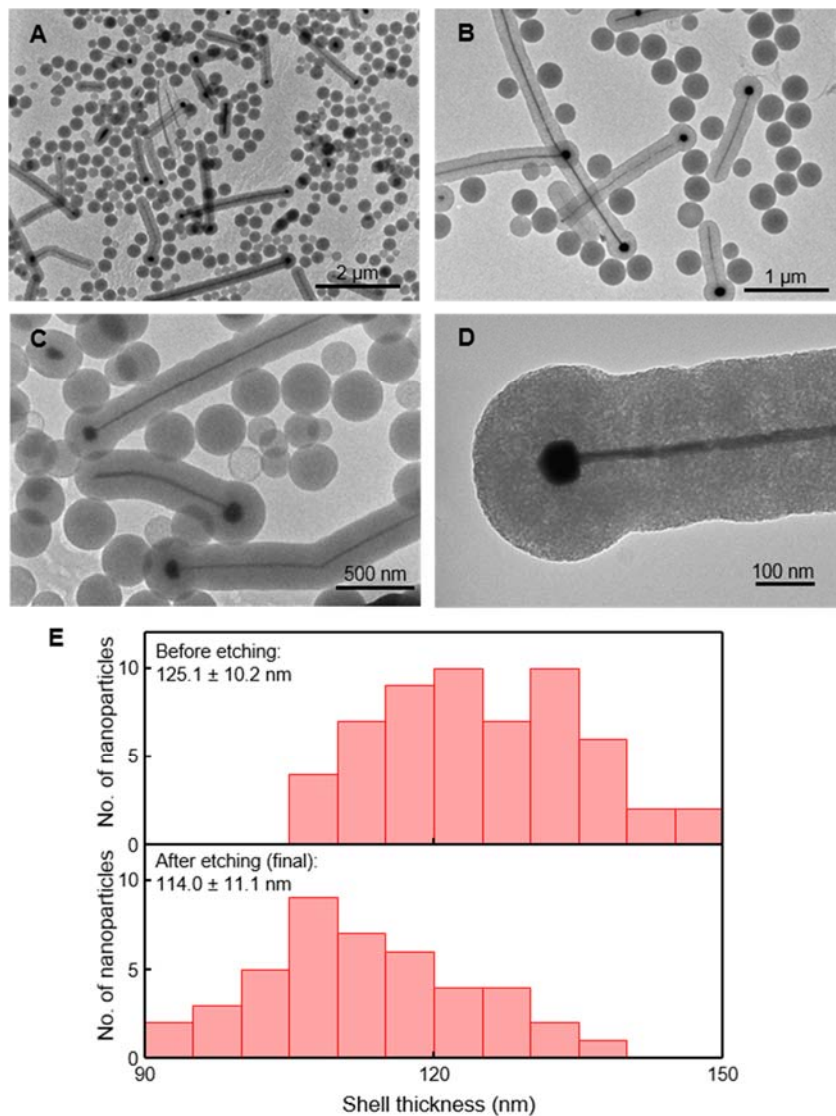
Figure S2. Structure characterizations of PdAu nanoparticles after silica shell coating and etching. TEM images of silica-coated PdAu nanoparticles (**A**, **C**) and mesoporous-silica-coated PdAu nanoparticles (after NaBH$_4$ treatment) (**B**, **D**). (**E**) Distributions of the silica-shell thickness before (top) and after (bottom) etching.

The mesoporous silica shell facilitates the fluorescent detection. In the super-resolution catalysis imaging experiment, the product molecules were detected while adsorbed within the mesoporous silica before they desorbed and disappeared into the surrounding solution. This is supported by the following experimental observations:

(1) In our previous study[6], we showed that the product resorufin desorption rate constant on Au nanoparticles increases with larger particle size, and reaches to >10 s^{-1} (i.e., faster than the timescale of 100 ms) when the particle size is > 13 nm. For the Au nanoparticle component in the PdAu nanoparticle, it is ~100 nm in diameter, much larger and thus the product desorption is expected to be fast.

(2) We could not detect stationary product molecules adsorbed on the PdAu nanoparticle without the mesoporous shell coating, likely because product desorption is faster than our image time resolution (20 ms). Another possibility is fluorescence quenching of the product directly on the metal surface, which we believe likely occurs but do not have quantitative measurements on. We therefore have come up with this mesoporous silica shell to facilitate the fluorescent detection, initially employed in a previous study[2].

(3) The dwell times (Figure S12F) and fluorescence intensities (Figure S12D) of the detected product molecules are all about the same on Pd and Au, which supports that, when imaged, the fluorescent products were trapped in the mesoporous silica shell rather than directly bound to the metal surface. Otherwise, we would expect to see some differences in the dwell times and fluorescence intensities of the product molecules on Pd and Au, due to possible differences in binding affinities and/or fluorescence enhancement or quenching on different metals.

(4) The catalysis mapping (main text, Figure 2A and C) shows that perpendicular to the long-axis of the PdAu nanoparticle, many detected product molecules reside clearly in the mesoporous shell region, away from the particle core. Since the total diameter (core + shell) of the particle is ~260 nm, significantly larger than our imaging resolution (~30-40 nm), these detection locations in the shell region directly support that the products adsorb onto silica-based sites within the mesopores.

Furthermore, the saturating kinetics of the concentration titration (main text, Figure 2G) indicates that the catalysis is metal-surface mediated and the mass transport in the mesoporous silica shell does not limit reaction kinetics (otherwise a linear dependence on reactant concentration is expected).

2.3 PdAu nanoparticles with built-in nanoscale gaps in mesoporous silica shell

The as-made mesoporous-silica-coated PdAu nanoparticles were heated at 450 °C for 1 h to break the Pd-Au junction (Figure S3A, B). After the heat treatment, the sample was also treated with NaBH$_4$ to reduce potential surface oxide layer. The gap size between Pd and Au varied broadly with the average of about 19 ± 11 nm (Figure S3C-D), which is larger at longer heat treatment time (Figure S3E).
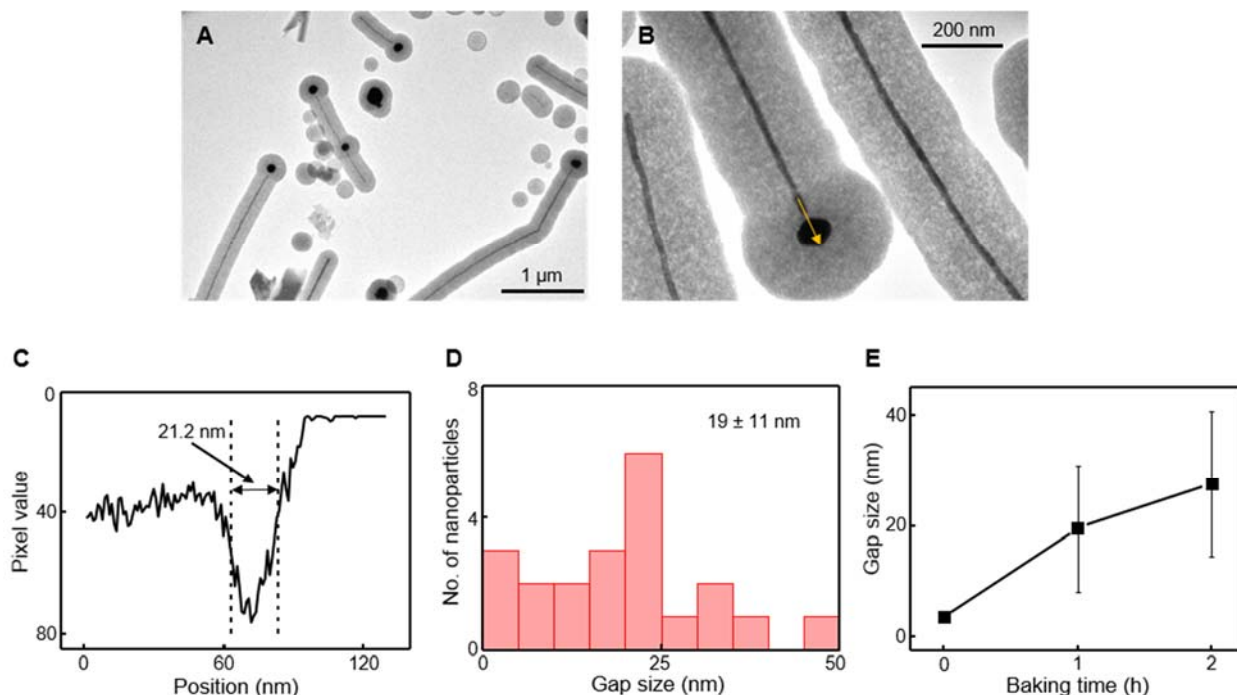
Figure S3. Structural characterizations of mesoporous-silica-coated PdAu nanoparticles after heat treatment to generate a gap. (**A**, **B**) TEM images of mesoporous-silica-coated PdAu nanoparticles with built-in nano-sized gaps. The arrow in B shows the direction of a line profile, which is presented in (C). (**C**) Line profile from B. The gap size is defined as the distance between the points at half-of-the-maximum for both sides. (**D**) Distribution of the gap size between Pd nanorod and Au particle after 1 h heat treatment. (**E**) Gap size versus heat treatment time. The error bar is s.d. The apparent gap size of ~3 nm at zero baking time indicates the uncertainty in measuring the gap size via line profiling the TEM images. This uncertainty is much smaller than the average gap size of 19 ± 11 nm from D.

3. The study of photo-driven disproportionation reaction of resazurin to resorufin

3.1 Pd and Au can catalyze the photo-driven disproportionation reaction

The ensemble activity measurement of the photo-driven disproportionation reaction of resazurin to resorufin was performed by taking the time-dependent fluorescence spectra of the reaction solution. We sealed ~10 µL reaction solution containing resazurin, phosphate buffer and catalysts (homemade Pd nanorods or Au nanoparticles) in a 1.5 mm diameter borosilicate glass tube (Sutter Instrument) and the solution was illuminated by either 5 mW 532 nm (Coherent Sapphire) or 50 mW 488 nm (CrystaLaser) laser to drive the catalytic reaction. The detailed experiment conditions are in Figure S4 caption. Note: the as-synthesized Pd nanorods were capped by ligands and inactive for catalysis. We thus used the surfactant free Pd nanorods for ensemble activity measurement: we heat-treated mesoporous-silica-coated Pd nanorods (which were made by coating the Pd nanorods with the same procedure as described for PdAu nanoparticles) to remove surfactants and then dispersed them into 0.1 M $NaBH_4$ for an extended period of 3 h to reduce the palladium oxide formed in calcination as well as to dissolve the mesoporous silica shell (due to the strongly basic $NaBH_4$ solution), which exposed more Pd surfaces for catalysis. The Au nanoparticles were sub-10 nm sized, citrate-capped, prepared by the standard citrate-$NaBH_4$ reduction method[7].

The ensemble activity measurements show that: 1) Both Pd and Au can catalyze the reaction (Figure S4A, B). 2) Without the catalyst or the 532 nm light excitation, the reaction is significantly slower and almost negligible compared with that in the presence of both catalyst and light (Figure S4C, D). 3) The reaction could not be driven by 488 nm light (Figure S4C, D), which supports that it is the excited-state resazurin rather than the excited metal involved in the reaction because 488 nm cannot excite resazurin efficiently but can excite metal valence electrons (Figure S4E).

Ensemble activity measurement of Pd nanorods   Ensemble activity measurement of Au nanoparticles
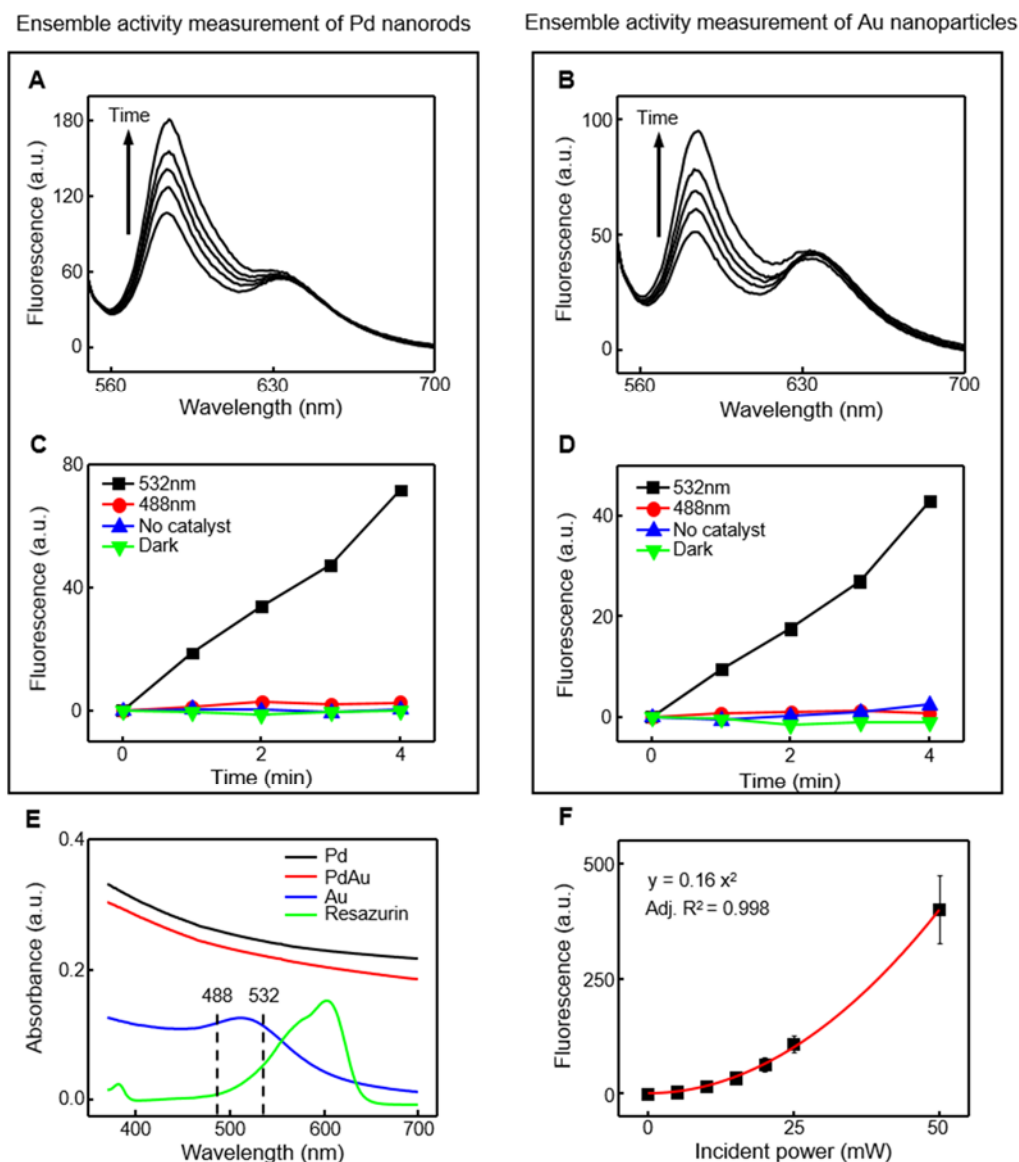
Figure S4. Ensemble catalytic activity measurement of Pd nanorods and Au nanoparticles. (**A**) Fluorescence spectra of the reaction solution containing 86.4 μM resazurin in 0.2 M pH 7.2 phosphate buffer in the presence of Pd nanorods under 5 mW 532 nm laser illumination. The fluorescence spectra were measured every 1 min and the increase of fluorescence at 583 nm indicates the formation of resorufin. (**B**) Same as A, but using Au nanoparticles as catalysts. (**C**) The time profile of fluorescence intensity at 583 nm of the reaction solution under conditions including: 1) with catalyst (Pd nanorods) under 5 mW 532 nm illumination (black), 2) with catalyst under 50 mW 488 nm illumination (red), 3) without catalyst under 5 mW 532 nm illumination (blue) and 4) with catalyst but no illumination (green). (**D**) Same as C but using Au nanoparticles as catalysts. (**E**) Absorbance spectra of Pd nanorods (black), PdAu nanoparticles (red), Au nanoparticles (blue) and resazurin solution (green). All particles were measured without silica shell. (**F**)

Power dependence of the uncatalyzed reaction activity (no catalyst added), which is reflected by the increase of fluorescence at 583 nm after 1 min reaction. The uncatalyzed reaction was measured in a more concentrated solution containing 0.78 mM resazurin in 0.2 M pH 6.6 phosphate buffer (lower pH here makes reaction faster and thus more easily measured). The error bar is the s.d. The excitation wavelength of all the fluorescence emission spectra is 532 nm.

3.2 Stoichiometry of the disproportionation reaction

The stoichiometry of the photo-driven disproportionation reaction of resazurin to resorufin was determined by quantitative analysis of the fluorescence spectra in the ensemble activity measurement. Here we used the above Pd-nanorod-catalyzed reaction (Figure S4A) to illustrate the stoichiometry measurement. The fluorescence spectra of pure resazurin (after TLC purification) and resorufin solution were shown in Figure S5A, which served as the standards to convert the fluorescence intensity into concentration. Note the fluorescence of the reactant resazurin is very weak, and needs to be measured at a much higher concentration. By monitoring the evolution of fluorescence at 583 nm and 634 nm along the reaction, we can get the relative concentration change of resazurin to resorufin (Figure S5B). It is worth noting that the fluorescence at 583 nm is from merely resorufin but at 634 nm is from the combination of resazurin and resorufin because of the spectral overlap. Therefore, for resazurin quantification (measured at 634 nm), we first removed the resorufin component (blue line in Figure S5B) and then calculated the concentration change. We measured the slope of the fluorescence intensity vs. time profile and converted that into resorufin generation or resazurin consumption rate. In the Pd-nanorod-catalyzed reaction, we calculated the stoichiometry of resazurin to resorufin is 3:1. In the same way, we also confirmed the stoichiometry of Au-nanoparticle-catalyzed reaction and the uncatalyzed reaction were 3:1 too.
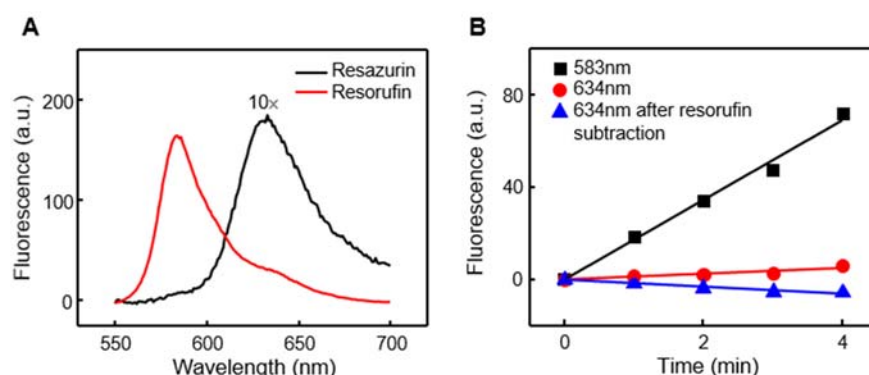
Figure S5. Stoichiometry determination of the photo-driven disproportionation reaction of resazurin to resorufin. (**A**) Fluorescence emission spectra of 1.03 μM resazurin (black, the curve is original data scaled by a factor of 10 to be clearly visualized) and 0.52 μM resorufin (red). (**B**) The fluorescence intensity versus time of the Pd-nanorod-catalyzed reaction solution at 583 nm (black), 634 nm (red), as well as 634 nm after subtracting the contribution of resorufin (blue). The stoichiometry of resazurin to resorufin was calculated to be 3:1.

3.3 Proposed mechanism of the uncatalyzed reaction

Previous studies showed resazurin excited at 532 nm can disproportionate into a one-electron-reduced and a one-electron oxidized species[8], and the one-electron-reduced species can further disproportionate into resorufin and resazurin[9]. Combining these previous results with our experiment results, we proposed the following mechanism of the uncatalyzed photo-driven disproportionation reaction of resazurin (Rz^-) to resorufin (Rf^-):

9

$$2Rz^{-*} \xrightarrow{\ k_1\ } Rz^\bullet + Rz^{2-\bullet} \tag{S3.1}$$

$$\underline{2Rz^{2-\bullet} + 2H_2O \xrightarrow{\ k_2\ } Rz^- + Rf^- + 2OH^-} \tag{S3.2}$$

$$\text{Overall: } 3Rz^- + 2H_2O \xrightarrow{\ h\nu\ } Rf^- + 2Rz^\bullet + 2OH^- \tag{S3.3}$$
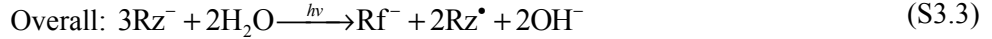
k_1 and k_2 are rate constants of reactions (S3.1) and (S3.2), respectively.

In this mechanism, the excited resazurin (Rz^{-*}) can form a one-election-oxidized ($Rz^\bullet$) and a one-election-reduced radical species ($Rz^{2-\bullet}$) through self-quenching (Eq. (S3.1)), which was reported by Encinas et al.[8] The one-election-reduced species ($Rz^{2-\bullet}$) can further disproportionate to resazurin (Rz^-) and resorufin (Rf^-) (Eq. (S3.2)), which was reported by Baldacchino et al.[9] The overall reaction (Eq. (S3.3)) shows the stoichiometry of resazurin to resorufin should be 3:1, which is consistent with our experimental observation (Section S3.2).

Based on this proposed mechanism, the rate law of the overall reaction can be described. As the photoexcitation of resazurin and its decay to the ground state is at ultrafast time scale, much faster than the kinetics of the reactions, the photoexcited species Rz^{-*} can be assumed to be in equilibrium with the ground state Rz^- under a constant light illumination condition. Therefore, the excited state resazurin concentration $[Rz^{-*}]$ should be proportional to the ground state resazurin $[Rz^-]$ and the incident power density I_0:

$$[Rz^{-*}] = K_{hv} I_0 [Rz^-] \tag{S3.4}$$

where K_{hv} is a proportionality constant.

Considering reactions (S3.1) and (S3.2), we applied the steady-state approximation to the one-election-reduced radical specials $[Rz^{2-\bullet}]$:

$$\frac{d[Rz^{2-\bullet}]}{dt} = k_1[Rz^{-*}]^2 - 2k_2[Rz^{2-\bullet}]^2 = k_1(K_{hv}I_0[Rz^-])^2 - 2k_2[Rz^{2-\bullet}]^2 = 0 \tag{S3.5}$$

Therefore

$$[Rz^{\bullet 2-}] = \sqrt{\frac{k_1}{2k_2}} K_{hv} I_0 [Rz^-] \tag{S3.6}$$

From reaction (S3.2), the resorufin $[Rf^-]$ formation rate is:

$$\frac{d[Rf^-]}{dt} = k_2[Rz^{\bullet 2-}]^2 = \frac{k_1}{2}(K_{hv}I_0[Rz^-])^2 = k_{eff} I_0^2 [Rz^-]^2 \tag{S3.7}$$

where $k_{eff} = \dfrac{k_1 K_{hv}^2}{2}$ is the effective rate constant.

This equation (S3.7) predicts a second-order power dependence of the uncatalyzed reaction rate, which was confirmed in the measurement of the power dependence of uncatalyzed reaction (Figure S4F). Note: since the uncatalyzed reaction is slow, we boosted the reaction by 1) increasing the resazurin concentration, 2) lowering pH of the solution, and 3) increasing the laser power. The results show that the reaction rate indeed has second-order power dependence.

It is worth noting that our results supports that the self-quenching (S3.1) is between two excited resazurin molecules, while in the earlier study this step was written as one excited resazurin interacted with a ground state resazurin[8].

4. Super-resolution catalysis imaging

4.1 Experiment setup

The super-resolution catalysis imaging experiment setup was described in our previous studies[2,3,10] (Figure S6A). The experiment was performed on a home-built prism-type wide-field total-internal-reflection fluorescence (TIRF) microscope (Olympus, IX71). A 25 mW circularly polarized continuous wave 532 nm light (CrystaLaser, GCL-025-L-0.5%) was focused on an area of $\sim 200 \times 100 \ \mu m^2$ in a home-made flow cell to excite the fluorescence of the catalytic product resorufin. The fluorescence was collected by a water-immersion 60X NA 1.2 objective (Olympus, UPLSAPO60XW), filtered by a 580 ± 30 nm band pass filter (Chroma, HQ580m60), and recorded by an EMCCD camera (ANDOR, iXon EM$^+$ DU-897 back illuminated) operating at 20 ms frame rate. For the single-particle emission spectrum measurement, we added a spectrograph (Princeton Instrument, Acton SP2150) in front of the EMCCD camera and took the spectrum of the product detected on a single catalyst particle to confirm the product is resorufin (Figure S6B).
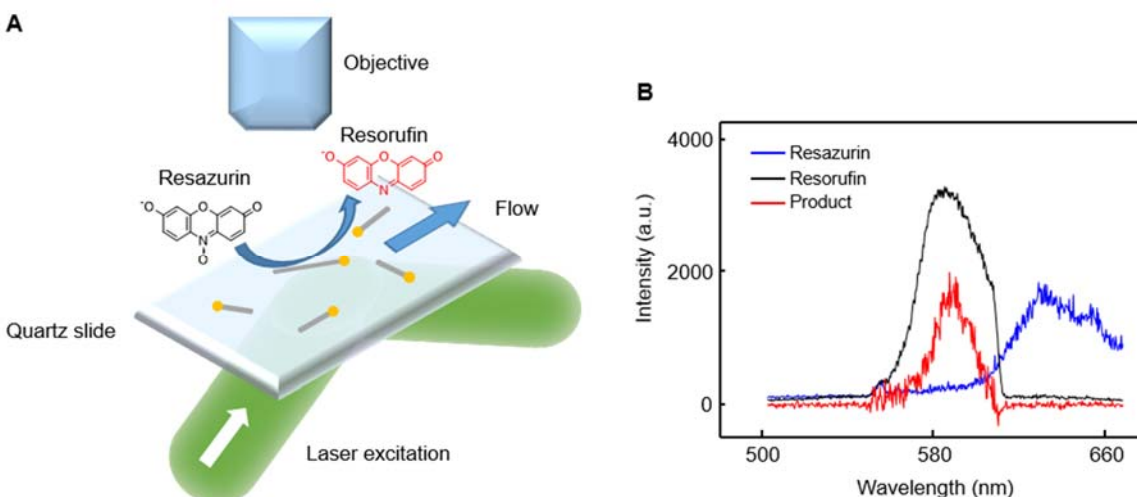

Figure S6. Super-resolution catalysis imaging on individual PdAu nanoparticles. (A) Schematic of experimental setup of the wide-field total-internal-reflection fluorescence (TIRF) microscope for super-resolution catalysis imaging. The prism on the back of the quartz slide and the coverslip on top of quartz slide were not shown. The configuration is depicted upside down here. (**B**) Single-particle fluorescence emission spectrum confirmed that the detected product was resorufin (red). The spectra of resazurin (blue) and resorufin (black) solutions were taken as references. The sharp vertical feature at 610 nm on the black spectrum was from the 580 ± 30 nm band pass cut off.

The flow cell was an assembly of a coverslip (Gold Seal) and a quartz slide (Technical Glass). Double-sided tape was used as the spacer in between to form a microfluidic channel, which was about 0.1 mm (height) $\times$ 5 cm (length) $\times$ 2 cm (width). Before assembly, a nanoparticle solution was drop-casted on the quartz slide and dried completely. During the experiment, the reactant (resazurin) solution was supplied into the channel with various concentrations (from 0 to 200 nM) at a continuous flow rate (50 μL min^{-1}) by a syringe pump (Chemyx), to give a steady-state reaction condition.

4.2 Analysis procedures of super-resolution catalysis imaging results

4.2.1 Identification of single molecule events

The fluorescence images were analyzed by a home-written Matlab program, iqPALM (image-based quantitative photo-activated localization microscopy), which was reported in our previous studies[10,11]. There were some modifications of the original program for the current work and the details are listed below.

(1) Each image was background subtracted (the average of the last 100 frames before each image was used as the background; note that the contribution of single-molecule signals to the background is negligible because typically in 100 frames there were typically less than 3 frames containing single-molecule fluorescence signals on a particle, and thus after averaging, their signals were completely washed out in the noise) to remove the constantly bright objects such as gold nanoparticle position makers, and the pixels with local maximum intensity larger than a threshold (typically mean plus 6 standard deviations of pixel counts in the image frame of 400×200 pixel^2, about 100×50 μm^2) were identified as the potential single molecule fluorescence signals. The threshold was intentionally set low to pick much more candidates (about 50) than the real events (less than 5) in each image frame and the later filtering process will clean up those false detections.

(2) For each picked pixel (i.e., local maximum), a 13×13 pixel^2 area (centered at that pixel) in the original image (without background subtraction) was taken out; from it we subtracted the same area of image from the average of the last five frames, which served as the background (if there was a local maximum found in these five frames, we used even earlier frames). By using the average of just 5 frames, we minimize the error in the background subtraction from stage drifting. Then the area was fitted with a 2-dimensional Gaussian function to get the centroid position (x, y). The fitting also generated the width parameters σ_x, σ_y (the standard deviations of the 2-D Gaussian function), integrated intensity (i.e., brightness) V of the Gaussian function as well as the localization errors Er_x, Er_y of the centroid position. The fitting details could be found in our earlier studies[2,11]. The drift correction was applied every frame based on the positions of 100 nm gold particle position markers (Ted Pella, Cat no. 82160-100), which are tannic acid-capped and inactive in catalysis. The positions of the makers were generated by fitting their emission signals with 2-D Gaussian functions.

(3) To clean up the false detections in the above analysis procedures, we filtered the fitted events by their σ_x, σ_y, Er_x, Er_y. The ideal fluorescence signal of a single resorufin molecule should appear with the diffraction-limited FWHM $0.61 \times \lambda/NA = 0.61 \times 583$ nm $/ 1.2 = 297$ nm, which is about 126 nm in σ_x, σ_y for a 2-D Gaussian function. The actual σ_x, σ_y of detected signal are peaked at ~197 nm (Figure S7A, B); this broadening is commonly seen, likely due to imperfect focusing of the detection system, noise contribution to the image, and that molecules are not exactly in the focal plane. Therefore we chose the events with σ_x, σ_y larger than 120 nm, and we also removed the events with σ_x, σ_y larger than 400 nm, which were too broad and negligible in population. We also applied the localization error filter to remove those events with Er_x, Er_y larger than 50 nm, which were bad fits and also small in population (Figure S7C, D). The summaries of the fitting parameters of σ_x, σ_y, Er_x, Er_y and integrated intensity V of the final catalytic events on PdAu nanoparticles are shown in Figure S7.
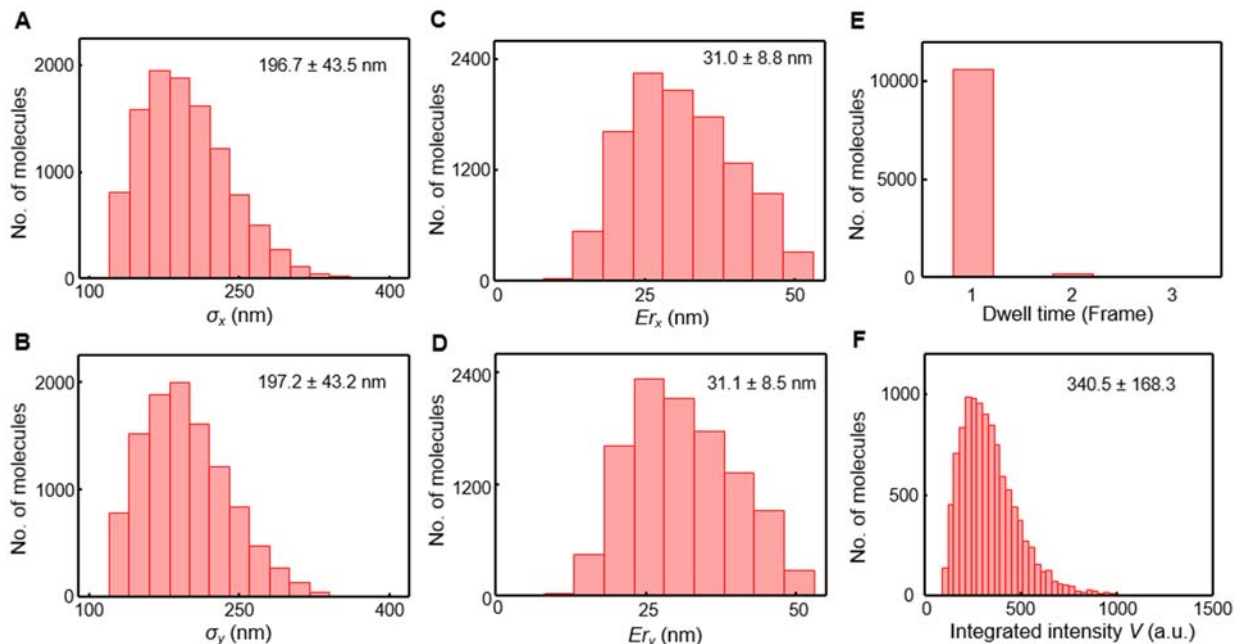
Figure S7. Obtained parameters of the detected product molecules. Distributions of σ_x (**A**), σ_y (**B**), Er_x (**C**), Er_y (**D**), dwell time (**E**), and integrated intensity of the 2D-Gaussian function V (in EMCCD camera counts) (**F**) of the detected molecules. The data contains 10853 events detected on 12 PdAu nanoparticles.

Justification of no over-counting for multi-frame events. Based on the iqPALM algorithm, if a fluorescence event lasts for several frames, it generates one fit per frame and therefore there might be an over-counting issue. To correct for it, we regarded the events in consecutive frames as the same molecule if they appeared within 50 nm in distance, which is approximately the mean plus 2 standard deviations of Er_x, Er_y. After event combining, we checked the dwell time of the detected single molecule events. Majority (98.1%) of the detected events only lasted for 1 frame (Figure S7E). It means the over-counting issue is negligible (<2%), but we corrected for it anyway. The short dwell time also means there is no significant lateral diffusion of the product molecule within the mesoporous silica shell before it desorbs and disappears into surrounding solution, which was also shown in our previous study through direct single product molecule tracking measurements (SI Figure S13 in reference[3]).

4.2.2 Corrections of detection efficiency

Correction of differences in reactant concentration. With the increase of resazurin concentration, the fluctuation of fluorescence background (noise) also increases, and the detection of weaker signals would be harder and the detection efficiency of the fluorescent product molecules could decrease. To correct for that, we used the movie taken at the lowest resazurin concentration (10 nM) as the reference to evaluate the decrease of detection efficiency at higher concentrations. The procedure is as follows (we used the correction for the movie taken at 20 nM resazurin as an example):

(1) Get brightness (mean) and noise (standard deviation) of each pixel from its time-based trajectory in the reference movie (10 nM) and the evaluation movie (20 nM). For pixel i in the reference movie, its pixel counts follow approximately a Gaussian distribution, $N(\mu_{i1}, \sigma_{i1}^2)$ and in the evaluation movie it should follow another Gaussian distribution, $N(\mu_{i2}, \sigma_{i2}^2)$, where μ is the mean value and σ is the standard deviation of the Gaussian distribution.

13

(2) Generate a simulated movie of 20 nM by adding noises to the reference movie. Every pixel i in the reference movie was adjusted by adding a Gaussian noise, $N(\mu_{i2} - \mu_{i1}, \sigma_{i2}^2 - \sigma_{i1}^2)$, so it followed the same distribution as that in the actual evaluation movie (20 nM) after adjustment. This means in the simulated movie, the brightness and noise of each pixel is close to that in the actual evaluation movie.

(3) Analyze the simulated movie and calculate the recovery ratio, which is defined as the number of events identified in the simulated movie normalized by that in the reference movie. The recovery ratio is used to correct for the detection efficiency decrease

Correction for differences in laser power. With the decrease of the incident laser power density, the signal-to-noise ratio of fluorescence events gets smaller so the detection efficiency also decreases. The difference between correcting for reactant concentration and correcting for laser power is: in the former case it is the increased noise leading to the decrease of detection efficiency, while in the latter, it is the decreased signal resulting in the decrease of detection efficiency. Therefore we have to use a different approach to evaluate the detection loss caused by the incident power decrease. To keep consistent with the correction for reactant concentration, we used the same reference movie (10 nM resazurin, 21.7 mW incident power) to evaluate relative detection loss at lower incident powers. The procedure is as follows (we used the correction for the movie taken at 16.9 mW incident light as an example):

(1) We examined the fitting results of the single molecule events (Figure S7) and recorded the distributions of fitting parameters as well as the noise at different power densities, which will be used to construct the simulated movie.

(2) Generate a simulated movie of 16.9 mW starting by constructing a series of fluorescent signals (2D Gaussian functions) on a flat surface with no noise. The brightness (V) and width (σ_x, σ_y) of the generated signals sampled their measured distributions from the actual movie (16.9 mW). Then add Gaussian noises to each pixel so that the noise in the simulated movie was close to that in the real movie.

(3) Analyze the simulated movie and calculate the recovery ratio, which is defined as the number of events identified in the artificial movie divided by the input number of single-molecule fluorescent signals. Finally the recovery ratios at different power densities were normalized by that in the reference movie (21.7 mW).

By evaluating the detection efficiency within the experimental reactant concentration and incident power range, we find: 1) With the increase of the reactant concentration, the detection efficiency dropped significantly (Figure S8A). At the highest substrate concentration (200 nM) the relative detection efficiency went down to 20% of that at 10 nM. 2) Within the experiment incident laser power range, the detection efficiency has very little change (Figure S8B). Therefore, we only applied the correction for the reactant concentration to the activity measurement (Figure S8C).
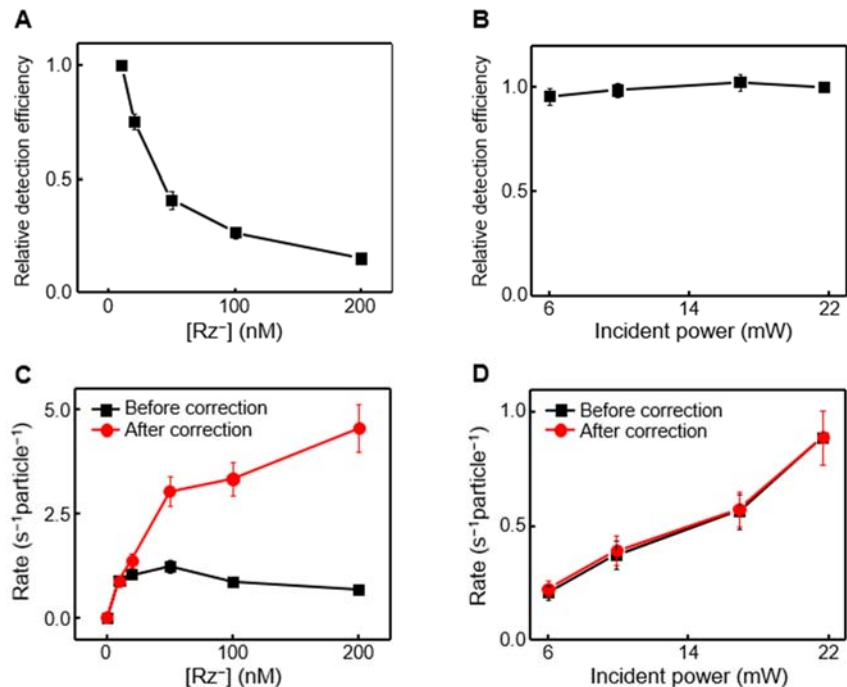
Figure S8. Correcting for the effect of reactant concentration and incident laser power density in affecting the detection efficiency. (**A**, **B**) The relative detection efficiency versus reactant concentration and incident power, respectively. (**C**) The concentration dependence of single PdAu nanoparticle turnover rates before (black) and after (red) correcting for the reactant-concentration dependent detection efficiency. (**D**) Same as C, but for correcting the laser incident power dependence; no significant difference here before and after the correction. The error bars are s.e.m.

4.2.3 Overlay of the super-resolution catalysis image onto the corresponding SEM image of PdAu nanoparticles

After we get the locations of the detected catalytic product formation events, we reconstructed the super-resolution (SR) image (i.e., 2-D histogram of product locations) of single particle catalytic activity. The SR image and SEM image were overlaid individually for every analyzed PdAu nanoparticle by the following procedures (Figure S9A). First, the SR and corresponding SEM images were both converted into binary images by thresholding (mean plus 2 standard deviations of all pixel values) to get the mass centers (of the binary images) and contours; the isolated hot pixels were removed from the binary image. We used this binary image, instead of the original SR image, to obtain the mass center because the mass center of the SR image could be affected by the activity heterogeneity at different locations within a single particle. Second, the contour from SR binary image was overlaid on top of that from SEM binary image with their mass centers overlapped. Third, the contour from SR image was rotated to maximize the overlap with the contour from SEM image. Note: In the subsequent spatial activity analysis, we only considered events within the SEM contour (with a 50 nm out-of-contour tolerance due to the spatial resolution of our catalysis imaging, ~40 nm).

The error of overlay. It is worth noting that each single particle overlay essentially establishes a transformation relation from the SR image to SEM image, which contains both translational and rotational moves. In the above overlaying process, the overall error has three components: 1) error in center determination in SEM image, 2) error in center determination in SR image and 3) error in rotation of SR image. The first term is related to the spatial resolution of SEM image (less than 5 nm), which is negligible

15

compared to the spatial resolution of catalysis imaging (~30-40 nm) thus we assumed the center position in SEM is perfectly determined. The second term, defined as Δr, is actually the error in translational move (because the overlay of mass centers was done by translation), which is about the spatial resolution of SR image (~30-40 nm, detailed evaluation shown in Figure S9B, C). The third term, defined as $\Delta\alpha$, is estimated ~1-2 degree (Figure S9B, C). Therefore the overall error is estimated ~40 nm within an area less than 2 × 2 μm^2; this area is larger than most of our particle sizes.

We evaluated Δr and $\Delta\alpha$ by the following procedures. We set the center of the overlaid particle as the reference point and used its transformation relation to check the overlay precision of the nearby particles (Figure S9B). For a nearby particle, the distance between its centers in the SR image and the SEM image, ΔD, is related to its distance from the reference point, r, through the equation $(\Delta D)^2 = (r\Delta\alpha)^2 + (\Delta r)^2 = r^2(\Delta\alpha)^2 + (\Delta r)^2$, where Δr and $\Delta\alpha$ are the radial (translation) and angular (rotation) errors (Figure S9B), which are orthogonal to each other. By linear fitting of $(\Delta D)^2$ vs. r^2 (Figure S9C), we can calculate Δr from the intercept Δr^2 and $\Delta\alpha$ from the slope $\Delta\alpha^2$. From the fitting results of 72 pairs of particles, we estimated Δr ~39 nm and $\Delta\alpha$ ~1.9 degree.

The high contrast of Au nanoparticle core in SEM image enables the direct size measurement. We measured the Au nanoparticle core size from SEM image and compared it to the result from TEM image (Figure S9D). The difference is about 10%, possibly due to that the small Au particles are not easily visible in SEM image. It is worth noting that the small difference of size measurement between SEM and TEM images would not affect the measured bimetallic activity enhancement because we only compared two Au hemispheres within the same particle, which share the same Au particle size.
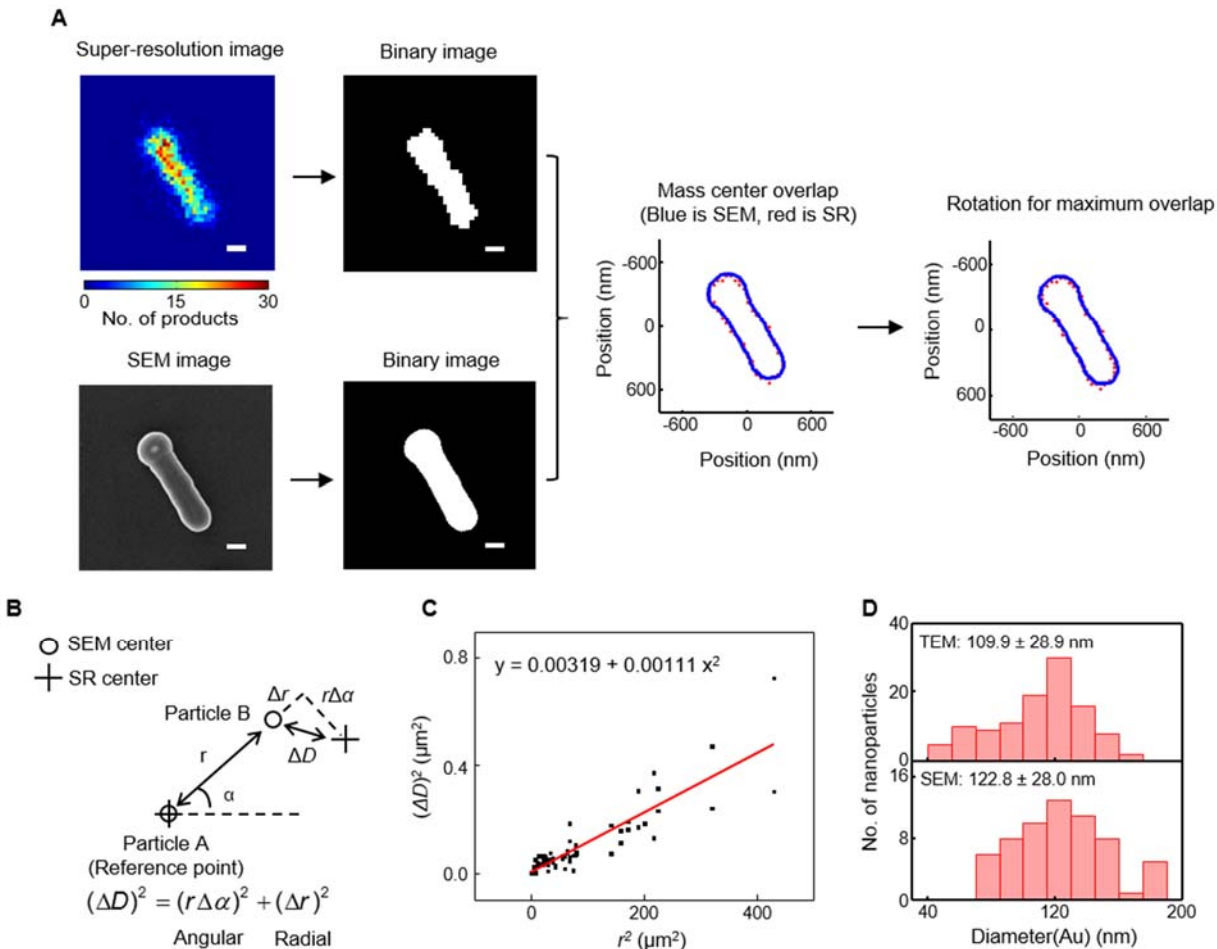
Figure S9. Overlay of the super-resolution (SR) catalysis image onto the SEM image of a PdAu nanoparticle. (**A**) Scheme of the overlay procedure. The SR and SEM images were converted into binary images to get their mass centers and contours. The mass centers were overlaid and then the SR image was rotated to achieve the maximum overlap of the contours in SR and SEM images. Since the original SR and SEM images were manually adjusted to have almost same orientations before overlay process, the rotation only did very small change (1.6 degree anticlockwise in this example shown). (**B**) The illustration of the overlay error. Particle A was set as the reference point to overlay the SR image onto SEM images. For a nearby particle B, the distance between its center in SR and SEM image (ΔD) is related to its distance from the particle A (r) as well as the radial (translation) error Δr and angular (rotation) error $\Delta\alpha$ of the overlay process. (**C**) $(\Delta D)^2$ versus r^2 for 72 pairs of particles to determine the overlay error. From the linear fitting, Δr (calculated from intercept) is 39 nm and $\Delta\alpha$ (calculated from slope) is 1.9 degree. (**D**) Size measurement of Au nanoparticle in PdAu nanoparticles from TEM image (upper) and SEM image (lower). The scale bars in the images represent 200 nm.

4.2.4 Additional examples of super-resolution imaging of activity enhancement at bimetallic regions.
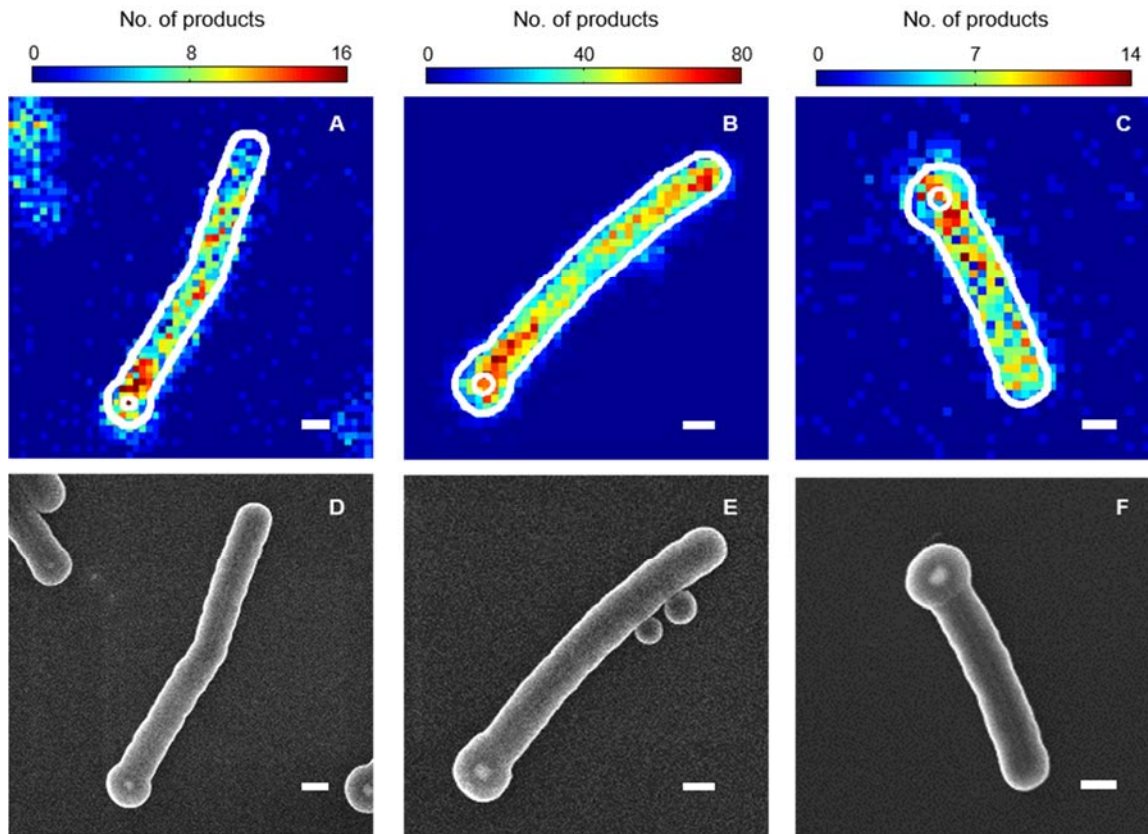
17

Figure S10. Additional examples of super-resolution catalysis imaging of catalytic activity enhancement near the Pd-Au bimetallic interface. (**A-C**) 2-D histogram of catalytic product positions on three PdAu bimetallic nanoparticles. (**D-F**) SEM images of the particles in A-C. All scale bars represent 200 nm.

4.2.5 Segmentation of the PdAu nanoparticles and surface area calculations

After we overlaid the super-resolution catalysis image onto the SEM image, we dissected the nanoparticle and the associated product positions into segmented regions for spatially resolved analysis. The segmentation is illustrated in Figure S11A. From the SEM image, we can locate the Pd-Au interface by using the center position and the diameter of Au nanoparticle. We defined the Pd segment (100 nm in length) next to the Pd-Au interface as the bimetallic Pd region (denoted as Pd_{Au}). For parallel comparison, the rest of the Pd nanorod was also dissected into 100 nm-long segments from the other free end (and the last segment is less than 100 nm because the rod length is not integer multiplication of 100 nm). All Pd segments except the free-end segment (Pd_{end}) and last two segments close to the interface (which covers the bimetallic Pd region, Pd_{Au}) were combined to be the monometallic Pd region (denoted as Pd). For Au nanoparticle, the hemisphere next to the Pd-Au interface was defined as the bimetallic Au region (Au_{Pd}) and the other hemisphere away from the bimetallic interface was defined as the monometallic Au region (Au).

In the gapped-PdAu nanoparticles, we also divided the Au nanoparticle into two hemispheres for comparison. The one proximal to the Pd nanorod was denoted as Au_p and the other hemisphere distant from the nanorod was labeled as Au_d.
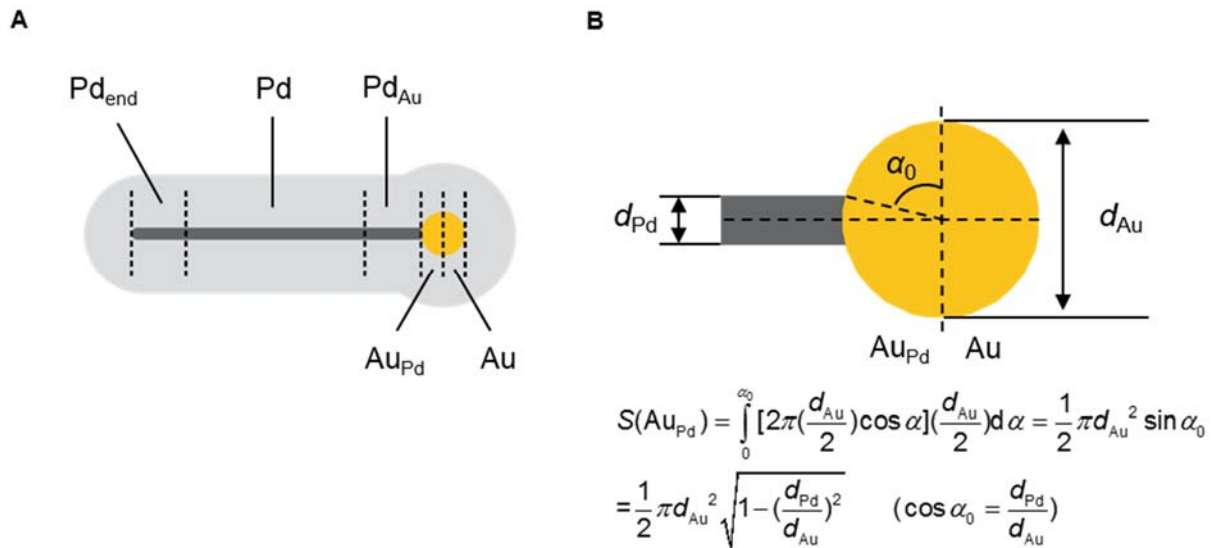
18

$$S(Au_{Pd}) = \int_0^{\alpha_0} [2\pi(\frac{d_{Au}}{2})\cos\alpha](\frac{d_{Au}}{2})d\alpha = \frac{1}{2}\pi d_{Au}^2 \sin\alpha_0$$

$$= \frac{1}{2}\pi d_{Au}^2 \sqrt{1-(\frac{d_{Pd}}{d_{Au}})^2} \quad (\cos\alpha_0 = \frac{d_{Pd}}{d_{Au}})$$

Figure S11. Segmentation of PdAu nanoparticles. (**A**) The model PdAu nanoparticle with the definitions of bimetallic regions (Pd_{Au}, Au_{Pd}), monometallic regions (Pd, Au) and the Pd end segment (Pd_{end}). (**B**) The surface area calculation of the bimetallic region Au_{Pd}, considering that its contact with the Pd nanorod is buried.

In order to evaluate the local specific turnover rates, we calculated the surface area of all regions (Table S1). Specifically, for the surface area of the bimetallic Au region (Au_{Pd}), we did not count the part of the Au hemisphere blocked by the contact with the Pd nanorod (Figure S11B), even though it is only a very small fraction — the difference between the Pd nanorod and Au particle diameters (for $d_{Pd} = 25$ nm and $d_{Au} = 110$ nm) is large and the blocked part is less than 3% of the hemisphere surface area.

Table S1. Surface area calculation of PdAu nanoparticles [a]

Regions	Pd_{Au}, Pd, Pd_{end}	Au_{Pd}	Au, Au_p [b], Au_d [c]
Surface area	$\pi d_{Pd}L$	$\frac{1}{2}\pi d_{Au}^2\sqrt{1-(\frac{d_{Pd}}{d_{Au}})^2}$	$\frac{1}{2}\pi d_{Au}^2$

[a] For bimetallic Pd region (Pd_{Au}) and monometallic Pd region (Pd), L is the segment length (100 nm). For the Pd end segment (Pd_{end}), L is the length of the end segment (100 nm), starting from the end of the Pd nanorod toward the rod body. [b, c] Au_p and Au_d refer to the Au hemispheres proximal to and distant away from the Pd nanorod in the gapped PdAu nanoparticles, respectively.

4.3 Control experiments

(1) <u>The catalytic activity of PdAu nanoparticles are stable over 6 hours</u>. We monitored the catalytic activity of the PdAu nanoparticles in the imaging experiment at $[Rz^-] = 50$ nM over 6 h and there is no obvious deactivation of the catalytic performance (Figure S12A).

(2) <u>Isolated monometallic Pd nanorods and Au nanoparticles show similar activities to the monometallic Pd region and the monometallic Au region in the bimetallic PdAu nanoparticles, respectively.</u> In our bimetallic PdAu nanoparticle sample, there are also pure Pd nanorods and Au nanoparticles present as minor components, which were imaged together with the bimetallic PdAu nanoparticles. The properties (rate constant and reactant adsorption equilibrium constant) of the pure monometallic particles are

comparable to the corresponding monometallic regions of the PdAu nanoparticles; this comparableness served as an extra control to show the increased activity of the bimetallic regions (Figure S12B, C).

(3) <u>The fluorescence intensity of the product resorufin is homogeneous across different regions within single PdAu nanoparticles</u>. We compared the fluorescence intensities of individual fluorescent product resorufin per image detected at different regions; there is no discernable difference among them (Figure S12D). This confirms that there is no detection bias between the bimetallic regions and monometallic regions.

(4) <u>Reactant accesses to the bimetallic and monometallic regions are equivalent.</u> To ensure that the observed catalytic activity differences at the bimetallic vs. monometallic regions are not due to differences in mesoporous silica shell structure (such as pore size) which could result in different access of the reactant to the metal surface, we flowed in the product resorufin solution and measured the binding frequency of the product molecules at different regions, using resorufin as a structural mimic to the reactant resazurin. For both Pd and Au, there is no appreciable difference in the observed binding frequency of resorufin between bimetallic regions and monometallic regions (Figure S12E), supporting there is no structural difference of the mesoporous silica shell and thus the accessibility of metal surfaces of different regions should be the same. Note we normalized the resorufin binding frequency by the corresponding mesoporous silica shell volume. The conclusion would not change if we normalize it by the corresponding metal surface area of different regions, because for the same length of Pd_{Au} and Pd segments (or Au_{Pd} and Au), they correspond to the same mesoporous silica shell volume as well as metal surface area (thus either way of normalization would give the same conclusion).

(5) <u>The dwell time of the product within the mesoporous silica shell is equivalent between the bimetallic and monometallic regions.</u> The dwell times of resorufin on the nanoparticles, which are due to adsorption to the sites within the mesopores of the silica shell, in the bimetallic regions and monometallic regions, are about the same (~20 ms, or 1 frame, Figure S12F). This comparable dwell time indicates that the trapping efficiency of the product by the mesoporous silica shell at different regions are approximately the same.
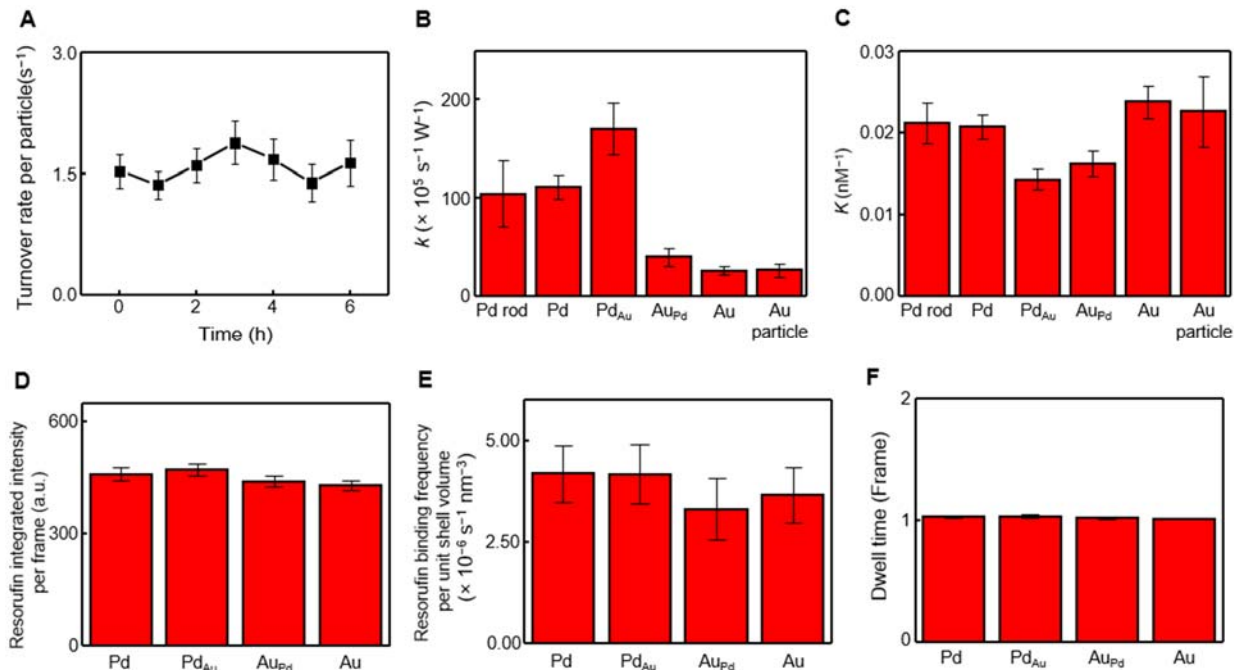
Figure S12. Control experiments of the super-resolution catalysis imaging of PdAu nanoparticles. (A) Temporal stability of the PdAu nanoparticle catalytic activity. The reaction condition is $[Rz^-]$ = 50 nM in 30 mM pH 7.2 phosphate buffer under 21.7 mW 532 nm laser excitation. Data averaged over 25 nanoparticles. (**B**, **C**) Rate constant k (B) and adsorption equilibrium constant K (C) of the bimetallic (Pd_{Au}, Au_{Pd}) and monometallic regions (Pd, Au) of the bimetallic PdAu nanoparticles in comparison with those of isolated monometallic Pd nanorods (Pd rod) and Au nanoparticles (Au particle) present in the sample (data averaged over 53 PdAu nanoparticles, 12 Pd nanorods, and 10 Au nanoparticles, respectively). (**D**) The integrated intensity per frame (in EMCCD counts) of the detected individual resorufin molecules at different regions (each region is an average from 20 PdAu nanoparticles). (**E**) The resorufin binding frequency per unit volume of the mesoporous silica shell at different regions (each region is the average result from 15 PdAu nanoparticles). The experiment was carried out under the condition $[Rf^-]$ = 190 pM in 20 mM pH 7.2 buffer under 21.7 mW 532 nm laser excitation. (**F**) Dwell time of the detected individual resorufin molecules at different regions. Each bar is an average of ~1000 events. All error bars are s.e.m.

4.4 Proposed kinetic mechanism of the catalytic reaction

Based on the reactant concentration and light power dependence of the single-particle catalytic activity shown in the main text (Figure 2F), we propose a kinetic model of the catalytic photo-driven disproportionation reaction of resazurin to resorufin. The resazurin concentration dependence follows a typical Langmuir adsorption isotherm, indicating the reaction occurs to catalyst-surface adsorbed resazurin. The linear light power dependence indicates the rate-limiting step should involve a photoexcited resazurin (in main text Section 2.1, we have presented results that support the photo-driven part comes from exciting resazurin rather than the photo-excited metal). Therefore, the conversion from resazurin to resorufin in our model is that a metal-surface-adsorbed excited-state resazurin $[M^n-Rz^{-*}]$ gets two electrons to be reduced to resorufin (reaction (S4.1); n reflects the number of electrons on the metal).

$$M^n-Rz^{-*}+H_2O \longrightarrow M^{n-2}-Rf^-+2OH^- \tag{S4.1}$$

This two-electron reduction could be two consecutive one-electron reductions with the 1st one being rate-limiting, but could also be simultaneous 2-electron reduction. We cannot differentiate these two possibilities at the moment, but we favor the former one considering the energetics of orbitals involved

(Figure S13A, right). Energetically, the singly-occupied HOMO of the excited-state resazurin can readily accept one, and only one, electron from the Fermi level of metal. The second electron transfer must occur after structural and electronic changes on the consequent 1-electron-reduced resazurin.

Based on this model, the specific turnover rate v (s^{-1} μm^{-2}) should be proportional to the concentration of adsorbed excited-state resazurin (as well as water, which could be from the bulk solution or adsorbed on the surface and which is a constant due to its large excess and can thus be part of the proportionality factor):

$$v \propto [M^n-Rz^{-*}] \tag{S4.2}$$

v should be further proportional to the incident power density I (in units of kW cm^{-2}) and the adsorbed ground-state resazurin $[M^n-Rz^-]$ since $[M^n-Rz^{-*}] \propto I[M^n-Rz^-]$:

$$v \propto I[M^n-Rz^-] \tag{S4.3}$$

The adsorbed resazurin $[M^n-Rz^-]$ should follow the Langmuir isotherm adsorption model, which is

$$[M^n-Rz^-] = \frac{n_T K[Rz^-]}{1+K[Rz^-]} \tag{S4.4}$$

where K (nM^{-1}) is the adsorption equilibrium constant of resazurin on the metal surface, and n_T is concentration of the total number of available surface sites. Therefore putting everything together we could the rate expression:

$$v = k'I \frac{n_T K[Rz]}{1+K[Rz]} = I\frac{kK[Rz]}{1+K[Rz]} \tag{S4.5}$$

where k' is a proportionality constant, and $k = k'n_T$ (in the units of s^{-1} W^{-1}) is effectively a rate constant that quantifies the catalytic reactivity of the metal. The unit of k does not contain μm^{-2} because the surface area normalization was included in the power density term I (in units of kW cm^{-2}). Equation (S4.5) predicts the linear light power density dependence and saturation behavior vs. resazurin concentration of catalytic activity, consistent with the experiment observations.

Reaction (S4.1) is the reduction half reaction of the overall disproportionation reaction. For the oxidation half reaction, which was not monitored directly in our experiments, a number of experimental observations hint on the underlying mechanism. First, since the stoichiometry of resazurin to resorufin in the reduction half is 1:1 while the overall stoichiometry of resazurin to resorufin was determined to be 3:1 (Section S3.2), the oxidation half should consume two resazurin molecules. Considering the reduction from resazurin to resorufin is an overall two-electron reduction reaction, the oxidation part should be two single-electron oxidations from two resazurin molecules in order to meet both stoichiometry and charge balance requirement. Second, from the energy level diagram (Figure S13A, left), the singly-occupied LUMO of the excited-state resazurin is energetically favorable to donate electron to Pd or Au. Combining these pieces of information, we proposed the oxidation half reaction as following (n reflects the number of electrons on metal):

$$M^n-Rz^{-*} \longrightarrow M^{n+1}-Rz^\bullet \tag{S4.6}$$

where $[M^{n+1}-Rz^\bullet]$ is the surface-bound one-electron-oxidized radical species from resazurin.

In this mechanistic model, the metal catalyst behaves like an electron mediator so it could donate/accept electrons to/from excited-state resazurin to facilitate the disproportionation reaction. Combining Equations (S4.1) and (S4.6), the balanced chemical equation for the overall reaction is then:
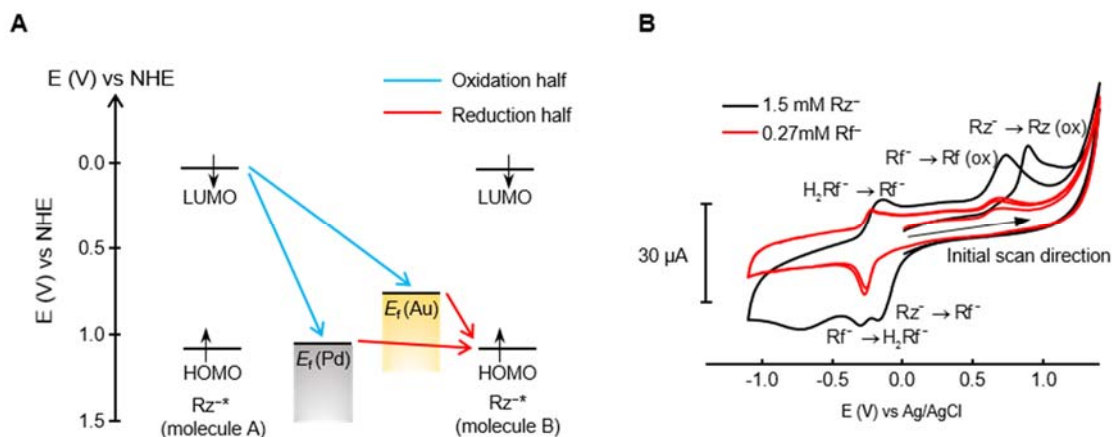
$$3Rz^- + H_2O \xrightarrow[hv]{M} Rf^- + 2Rz^\bullet + 2OH^- \tag{S4.7}$$
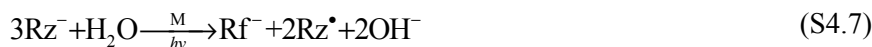
Figure S13. Energetics of the Pd/Au-catalyzed photo-driven disproportionation of resazurin to resorufin. (A) Energy level diagram of the HOMO and LUMO of resazurin and the Fermi level of Pd and Au; all referenced to the normal hydrogen electrode (NHE). The blue and red arrows refer to the oxidation and reduction pathways. The energies of HOMO (1.08 V) and LUMO (0.03 V) of resazurin were estimated from the electrochemistry measurement of resazurin, which were consistent with the DFT calculation results (E_{HOMO} = 0.99 V, E_{LUMO} = −0.34 V) **(B)** Cyclic voltammetry (CV) of 1.5 mM resazurin (black) and 0.27 mM resorufin (red) in 0.2 M pH 7.2 phosphate buffer. Scan rate = 25 mV s^{-1}; glassy carbon working electrode.

Cyclic voltammetry (CV) of resazurin and resorufin. As shown in Figure S13B, we measured the oxidation and reduction potentials of resazurin and resorufin. For resazurin (black): 1) the irreversible reduction wave with a peak potential at −0.18 V is the reduction of resazurin (Rz$^-$) to resorufin (Rf$^-$)[12], 2) the irreversible oxidation wave at 0.89 V is the oxidation of resazurin to an unknown product (Rz (ox)), 3) the reversible redox waves at −0.31 V and −0.15 V are from the resorufin (Rf$^-$) /dihydroresorufin (H$_2$Rf$^-$) redox couple,[12] and 4) the irreversible oxidation wave at 0.74 V is the oxidation of resorufin to an unknown species (Rf (ox)). For resorufin (red), expectedly, 3) and 4) regarding Rf$^-$/H$_2$Rf$^-$ reversible conversion and oxidation of resorufin appeared, further supporting our assignment. Note the measured reduction of resazurin (Rz$^-$) to resorufin (Rf$^-$) is a 2-electron process and the oxidation of resazurin to an unknown product (Rz (ox)) is also a 2-electron process (confirmed by the area under the peak). We approximated these two potentials as the energy levels of HOMO and LUMO. This approximation is valid by that they are close to the independent DFT calculation results (1.08 V vs. 0.99 V for HOMO, 0.03V vs. −0.34 V for LUMO; former from CV, latter from DFT).

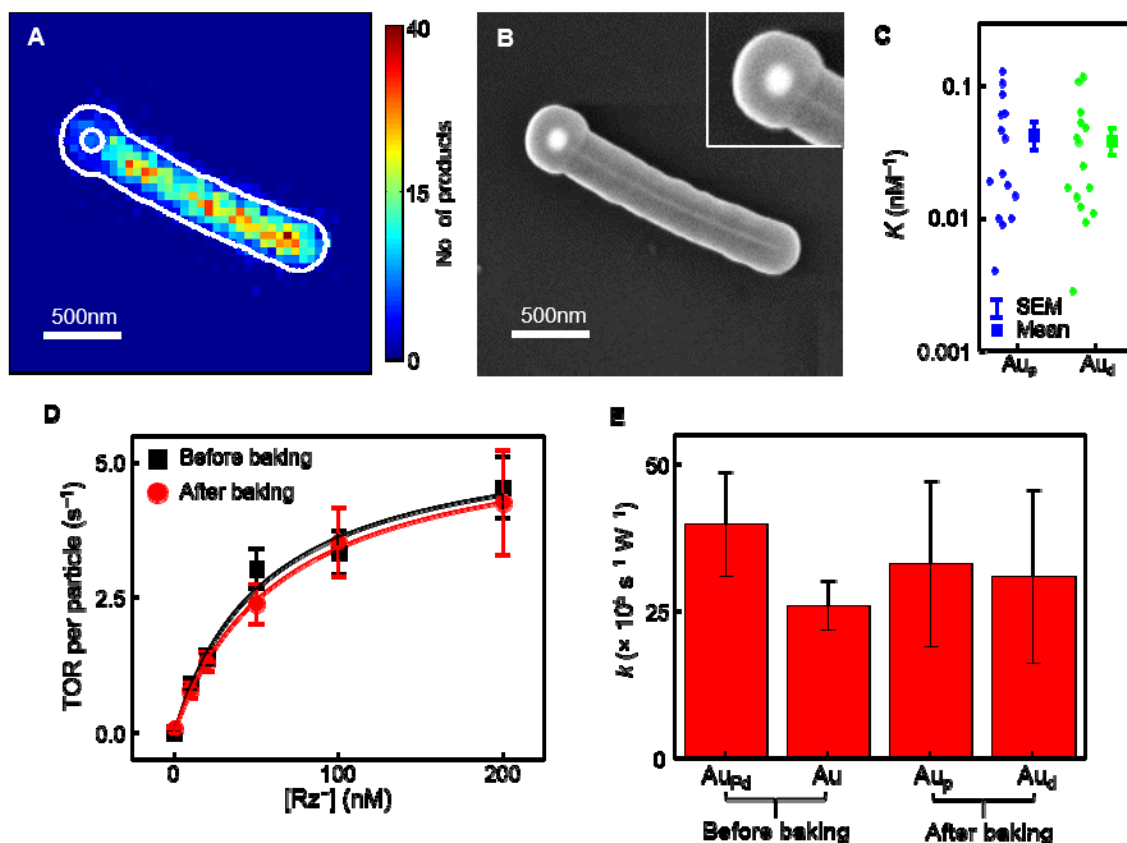4.5 Additional data: super-resolution catalysis imaging of the gap-PdAu nanoparticles

Figure S14. Additional super-resolution catalysis imaging results of gap-PdAu nanoparticles. (**A**) 2-D histogram of catalytic product positions on a gap-PdAu nanoparticle. (**B**) SEM image of the particle in A; the inset is the zoom-in of the nano-gap. (**C**) The adsorption equilibrium constant of the reactant K of the Au hemispheres proximal to (Au_p) and distant from (Au_d) the Pd nanorod in the gapped-PdAu nanoparticles. No appreciable difference is observed between two hemispheres. (**D**) Single-particle catalytic activity of mesoporous silica coated PdAu nanoparticles before and after 1 h heat treatment. The experiments were carried out at different resazurin concentrations under ~0.35 kW cm^{-2} 532 nm laser excitation. The results are averaged from 53 (before baking) and 20 (after baking) particles. (**E**) Catalytic rate constant k of the Au hemispheres before and after baking. Before baking: bimetallic (Au_{Pd}) and monometallic (Au) regions. After baking: Au hemispheres proximal (Au_p) to and distant (Au_d) from the Pd nanorod. Error bars: s.e.m.

5.FDTD simulations

5.1 Method

The 2D finite-difference time-domain (FDTD) simulations were performed to calculate the electric field intensity distribution on a PdAu nanoparticle surface, using a commercial software (Lumerical Solutions). The grid size was set 2×2 nm^2 and refractive index of the background medium was set as 1.33 (water). All the material properties were set based on the default optical material database (Palik). We used 532 nm circularly polarized light source (composed by two orthogonal linearly-polarized light sources with 90 degree phase difference) to excite a model PdAu nanoparticle, composed of a 120 nm diameter spherical Au particle attached to one end of a Pd nanorod of 400 nm in length and 30 nm in diameter. To mimic the

experiment configuration, the incident light propagation direction was fixed and the PdAu nanoparticle was rotated to cover all the possible orientations in the experiment. An exemplary FDTD simulation result is shown in Figure S15A, upper panel, in which the PdAu nanoparticle is parallel to the light propagation direction. Its orientation angle θ is 0°, based on the definition shown in the inset. Following the similar segmentation schemes as in the super-resolution catalysis imaging analysis, we defined the locations to calculate the electric field intensity enhancement ($|E|^2/|E_0|^2$) of the bimetallic (Pd_{Au}, Au_{Pd}) and monometallic (Pd, Au) regions (Figure S15A, lower panel). We only considered the locations within 2 nm of the metal surface because the catalytic reactions occur at the surface and the size of the reactant and product molecules are ~1 nm. As expected, the local $|E|^2/|E_0|^2$ is dependent on the particle orientation (Figure S15B; note that θ is varied every 15° from 0° to 180° and when $\theta > 180$°, it is equivalent to $(360-\theta)$° because of symmetry). So we calculated $|E|^2/|E_0|^2$ of the bimetallic and monometallic regions for each individual particle based on its actual orientation in the imaging experiment.
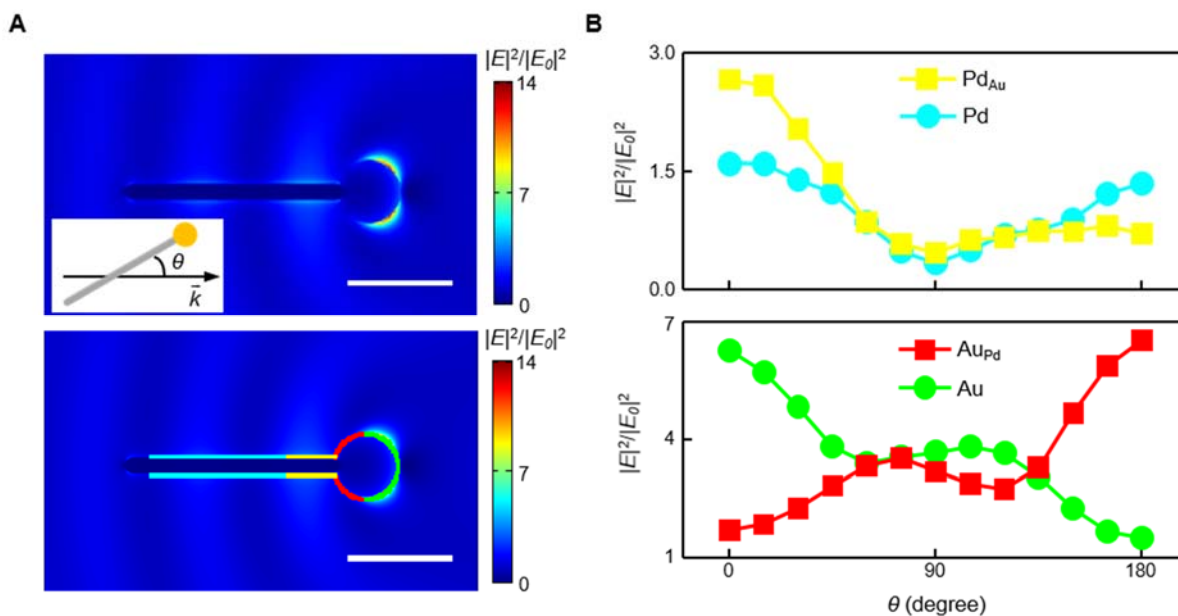

Figure S15. FDTD simulations of the PdAu nanoparticles. (**A**) Upper: the electric field intensity enhancement ($|E|^2/|E_0|^2$) pattern of the PdAu nanoparticle excited by 532 nm circularly polarized light with the propagation direction from left to right (shown in the inset). The inset in the upper panel shows the definition of the particle orientation angle θ with respect to the light propagation direction. For the PdAu nanoparticle presented here, $\theta = 0$°. Lower: The locations defined to calculate $|E|^2$ of the bimetallic regions, Pd_{Au} (yellow), Au_{Pd} (red), and monometallic regions, Pd (cyan), and Au (green). Only the near-surface (within 2 nm) region was considered in determining the $|E|^2/|E_0|^2$ for each region because both the reactant and product molecule sizes are ~1 nm. (**B**) $|E|^2/|E_0|^2$ of the bimetallic and monometallic regions versus particle orientation angle θ. The scale bars represent 200 nm.

5.2 No significant plasmonic effect in catalysis.

The FDTD simulations of the electric field intensity ($|E|^2$) pattern around the PdAu nanoparticle can be used to evaluate whether the surface plasmon excitation of Au nanoparticle by 532 nm laser light may or may not play a role in the observed catalytic enhancement around the Pd-Au interface. As shown in Figure S15A, the localized electric field enhancement is expectedly clear around the Au nanoparticle, while there is no significant enhancement near the Pd-Au interface or around the Pd nanorod, as 532 nm light does not excite Pd surface plasmon effectively. The $|E|^2$ ratios of bimetallic vs. monometallic regions, i.e., Pd_{Au}/Pd and Au_{Pd}/Au, for all possible particle orientations are shown in Figure S16A, upper. Taking

25

into account the actual orientations of all PdAu nanoparticles we examined (Figure S16A, lower), the weighted average of the $|E|^2$ enhancement for both Pd_{Au} vs. Pd and Au_{Pd} vs. Au are merely 12% and 4%, respectively, because most of the nanoparticles are within the orientation range of 30 to 150° where $|E|^2$ ratios for both Pd_{Au}/Pd and Au_{Pd}/Au are ~1. This $|E|^2$ enhancement is much smaller than the observed average activity enhancement (~50%; main text Figure 3A, lower). Moreover, no correlation was observed between the catalytic rate constant k ratio and the local $|E|^2$ ratio of the bimetallic to monometallic regions (Figure S17).

We further normalized the catalytic rate constant k of each segment by its local $|E|^2$ to factor out the potential contribution of local electric field enhancement. The resulting normalized k' of the bimetallic Pd_{Au} and Au_{Pd} regions are still ~50% and ~70% larger than those of the monometallic Pd and Au regions, respectively (Figure S16B). Taken together, these results indicate that plasmonic enhancement effect does not make a significant contribution to the observed catalytic enhancement at the bimetallic regions of the PdAu nanoparticles, even though the reaction is photo-driven.
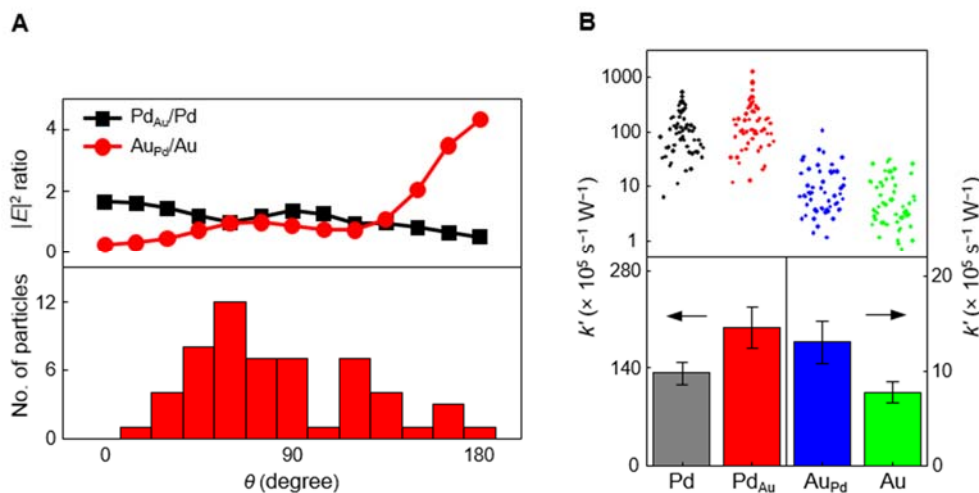

Figure S16. No significant plasmonic effect in catalysis. (**A**) Upper: the $|E|^2$ ratios of bimetallic vs. monometallic regions for Pd_{Au}/Pd and Au_{Pd}/Au as a function of particle orientation to the k-vector (light propagation direction). Lower: the orientation distribution of the PdAu nanoparticle examined experimentally. (**B**) The normalized catalytic rate constant k' of bimetallic and monometallic regions of individual PdAu nanoparticles after factoring out the local electric field intensity enhancement contribution (upper). Lower panel shows the particle-averaged values; error bars are s.e.m.
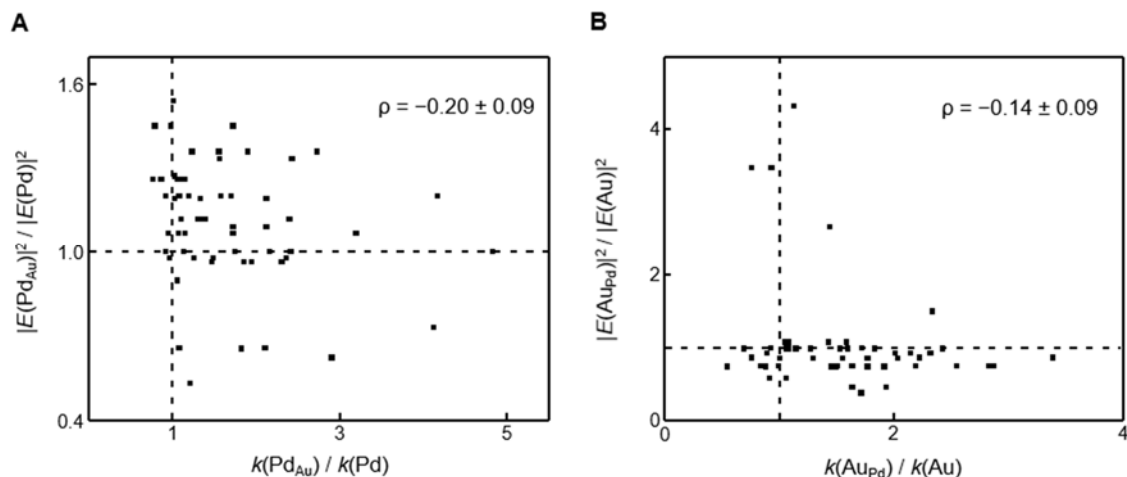
Figure S17. No correlation between the local electric field intensity and catalytic activity of PdAu nanoparticles. The correlation between the electric field intensity ($|E|^2$) ratio and catalytic rate constant (k) ratio of the bimetallic region over monometallic region, for Pd (**A**) and Au (**B**), respectively. Each dot represents a single PdAu nanoparticle (total 53). For each particle, the local $|E|^2$ of the bimetallic and monometallic regions were calculated based on its actual orientation in the experiment. The dashed vertical and horizontal lines go through (1, 1).

6.DFT calculations

6.1 Method

The DFT calculations of resazurin adsorption on Pd or Au surfaces were performed using the Vienna Ab initio Simulation Package (VASP, version 5.3.5)[13,14] in vacuum at 0 K. A plane-wave basis set of 400 eV energy cutoff was used with the Perdew–Burke–Ernzerhof (PBE) exchange-correlation functional[15,16] and the projector augmented wave (PAW) pseudopotentials[17,18]. The convergence criteria are 10^{-4} eV for the electronic relaxation and 10^{-3} eV for the ionic relaxation (i.e., geometry optimization). Dispersion correction was included by using the zero damping DFT-D3 method of Grimme[19].

For fcc Pd (100) and Au (111) surfaces, we used a 6 × 6 supercell of five layers (180 metal atoms in total) with a vacuum region of more than six layers to break the interactions between neighboring surfaces. The lattice constants of Pd and Au were set as 3.89 Å and 4.08 Å[20], respectively. We only sampled the Gamma point in k-space because the supercell is very big. Both the metal surface and resazurin molecule were first geometry optimized and then put together to calculate the adsorption geometry, in which we had one resazurin molecule (per supercell) on top of the metal surface and geometry optimized the system (only the resazurin molecule and the top surface layer of the metal atoms were allowed to relax). A series of initial locations and orientations of resazurin on the surface were considered on the basis of the symmetry and possible important atomic interactions; all the cases were geometry optimized and the most stable one in energy was treated as the final adsorption geometry.

To investigate bimetallic effects on the Pd-based and Au-based surfaces, we used single-atom-substitution by the second metal to construct bimetallic surfaces. Starting from Pd (100) or the Au (111) surface, we substituted the surface atom that was identified to be involved in the adsorbate-surface interaction. We substituted all the relevant single surface atoms, one at a time, and optimized resazurin adsorption geometries on each of the constructed bimetallic surfaces. The most stable one was used as the final adsorption geometry on the bimetallic surface. The bond lengths were directly measured from the

optimized geometries and the atomic charges were calculated by Bader's analysis, using the code developed by Henkelman et al[21,22].

The adsorption energy E_{ads} was defined as

$$E_{ads}=E_{slab}+E_{Rz}-E_{slab+Rz} \tag{S6.1}$$

where E_{slab} is the electronic energy of the metal slab (monometallic or bimetallic) without resazurin adsorption and E_{Rz} is the electronic energy of the free resazurin and $E_{slab+Rz}$ is the electronic energy of the metal slab with resazurin bound to the surface.

Crystal orbital Hamilton population (COHP) analysis[23,24] was performed to analyze the bonding interactions between Rz and the metal surface, using the Local-Orbital Basis Suite Towards Electronic-Structure Reconstruction package (LOBSTER, version 2.0.0)[25]. We specifically analyzed the interactions between the O or N atom of the N−O fragment of resazurin and the closest surface metal atoms (Pd or Au). In COHP and density of states (DOS) diagrams, the zero energy point refers to the vacuum level. Note in COHP analysis, the convention is that the *x*-axis represents the reserved COHP value, labelled as –COHP, in order to make the bonding interaction appear in the positive region and antibonding interaction in the negative region.

Molecular orbitals (MOs) of resazurin were calculated using Gaussian 09 software (Gaussian, Inc.) with PBE/SDDALL level of theory and the results were compared with the DOS of resazurin calculated from VASP.

6.2 Resazurin adsorption on monometallic surfaces

6.2.1 Resazurin on Pd(100) surface

We show the initial and the corresponding optimized geometries of resazurin on Pd(100) surface in Figure S18 (the red color labels the most stable geometry). Since the initial resazurin position on the surface may affect the final adsorption geometry, we started with ten initial resazurin positions to try to cover the most possible situations (left structure in each panel in Figure S18). First, we considered both flat-on (structures I to VIII) and edge-on (structures IX to X) adsorption geometries. For the edge-on geometries, we considered two candidates and each had a single O atom on top of a Pd atom. For the flat-on geometries, we consider two general molecular orientations: the long axis of resazurin's phenoxazine ring (indicated by the arrow in Figure S18, structure I) parallel to the edge (structures I to IV) and to the diagonal (structures V to VIII) of the supercell, which is a square from the top view. For each general orientation, the resazurin molecule was translated on the surface in order to form possible interactions with the surface atoms (i.e., atoms of resazurin to be directly on or close to be on-top of some metal surface atoms). The ten initial geometries were optimized (right structure in each panel in Figure S18) and the most stable one (structure III) is the flat-on configuration in which the Pd–C interactions dominate.
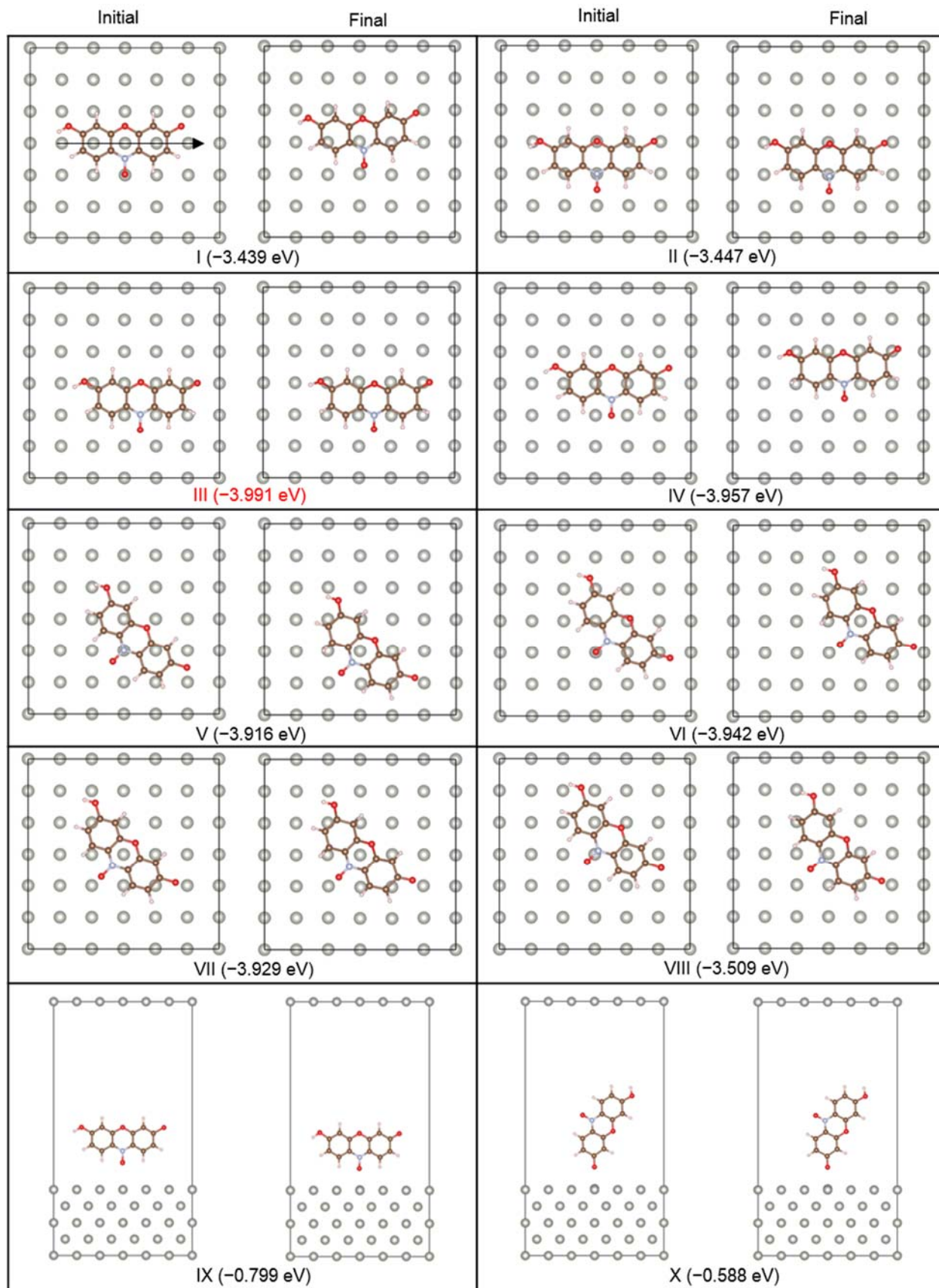
I (−3.439 eV)

II (−3.447 eV)

III (−3.991 eV)

IV (−3.957 eV)

V (−3.916 eV)

VI (−3.942 eV)

VII (−3.929 eV)

VIII (−3.509 eV)

IX (−0.799 eV)

X (−0.588 eV)

Figure S18. Initial (left) and optimized (right) geometries of resazurin on Pd(100) surface. Structures I-VIII are flat-on configurations and structures IX-X are edge-on configurations. The most stable candidate (structure III) was taken as the final adsorption geometry of resazurin on Pd(100) surface. The arrow in structure I is the long axis of the phenoxazine ring of resazurin.

6.2.2 Resazurin on Au(111) surface

Figure S19 presents the initial and optimized geometries of resazurin on Au(111) surface. Similarly, we consider flat-on (structures I-VIII) and edge-on (structures IX-X) configurations. For the flat-on ones, we considered two general molecular orientations: the long axis of phenoxazine ring (indicated by the arrow in Figure S19, structure I) along (structures I-II) the longer diagonal of the supercell, which is a rhombus from the top view; and along the edge of the supercell (structures III-V). From the optimized results of structures I-V, we found that the Au–O interaction is favorable as structure II was the most stable among the five structures. Therefore, based on structure II, the resazurin molecule was rotated around the O atom (which is on top of a Au atom) by 15° (structure VI), 30° (structure VII), 45° (structure VIII) to search for more stable geometries. Of all ten optimized geometries, structure II turned out to be the most stable one, in which the Au–O interaction is important.
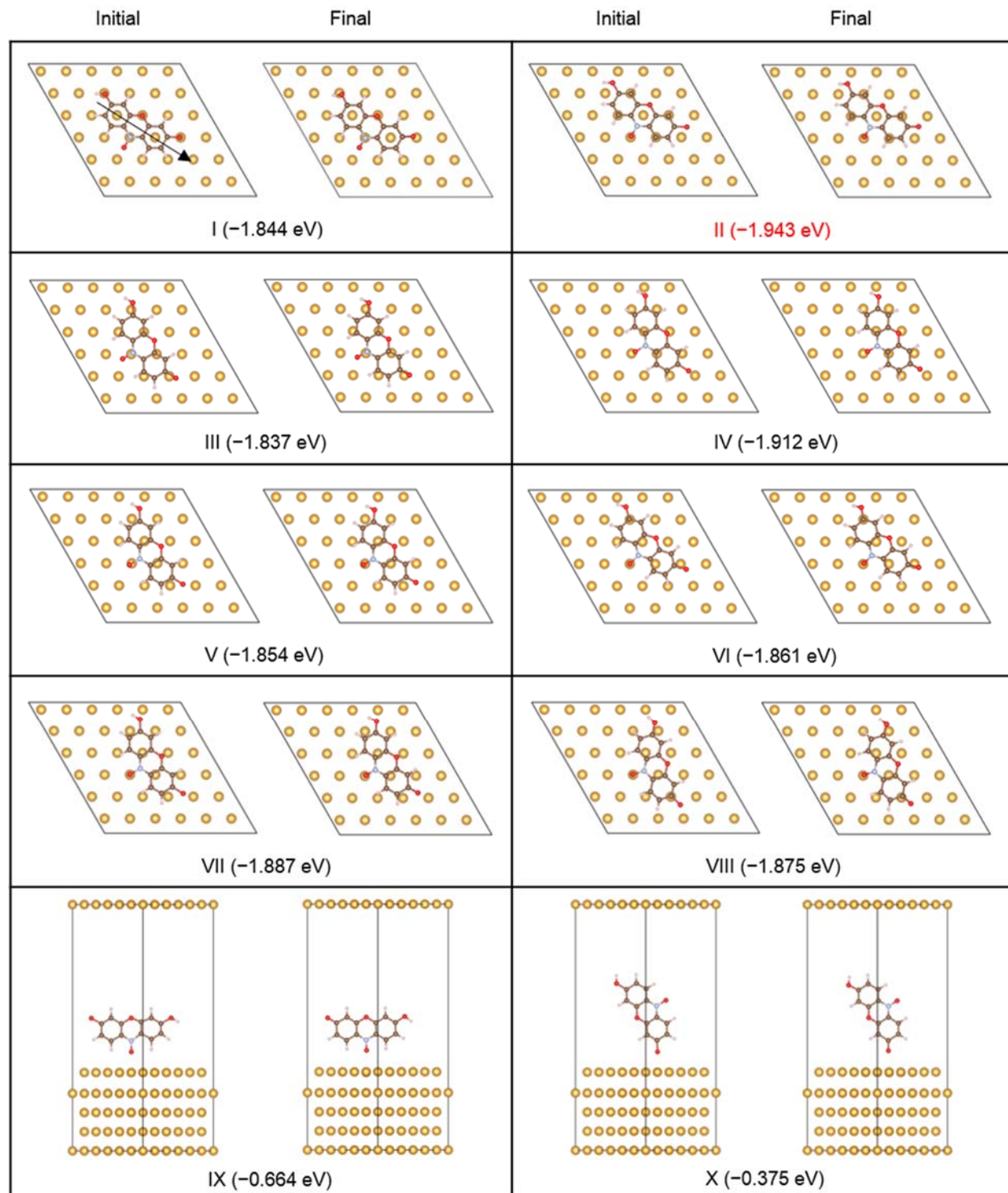
Figure S19. Initial (left) and optimized (right) geometries of resazurin on Au(111) surface. Structures I-VIII are flat-on configurations and structures IX-X are edge-on configurations. The most stable candidate (structure II) was taken as the final adsorption geometry of resazurin on Au(111) surface. The arrow in structure I is the long axis of the phenoxazine ring of resazurin.

31

6.3 Resazurin adsorption on bimetallic surfaces

6.3.1 Resazurin on Au@Pd(100) surface

Based on the most stable geometries of resazurin on Pd(100) (Structure III in Figure S18), there are eight surface Pd atoms dominating the interactions with resazurin (labelled 1-8 in Figure S20A). For each of them, we substituted it with a Au atom to construct the Au@Pd(100) bimetallic surface and subsequently optimized the adsorption geometry (Table S2). Among the eight substitution candidates, six substituted structures have equal or longer N–O bond length than that on Pd(100) surface. The substitutions at Pd atom no.2 and no. 8 are the two most stable ones (Figure S20B, C, E, F). We focus more attention on structure no. 2 since it has a more lengthened N–O bond (by 0.004 Å) compared with that on monometallic surface (Table S2), which means there is more N−O bond activation. Structure no. 8, although slightly more stable than structure 2 (by 0.006 eV), its N−O bond is shorter (by 0.003 Å) than that on Pd(100), reflecting a deactivation of the N−O bond, which makes it irrelevant for bimetallic enhancement.
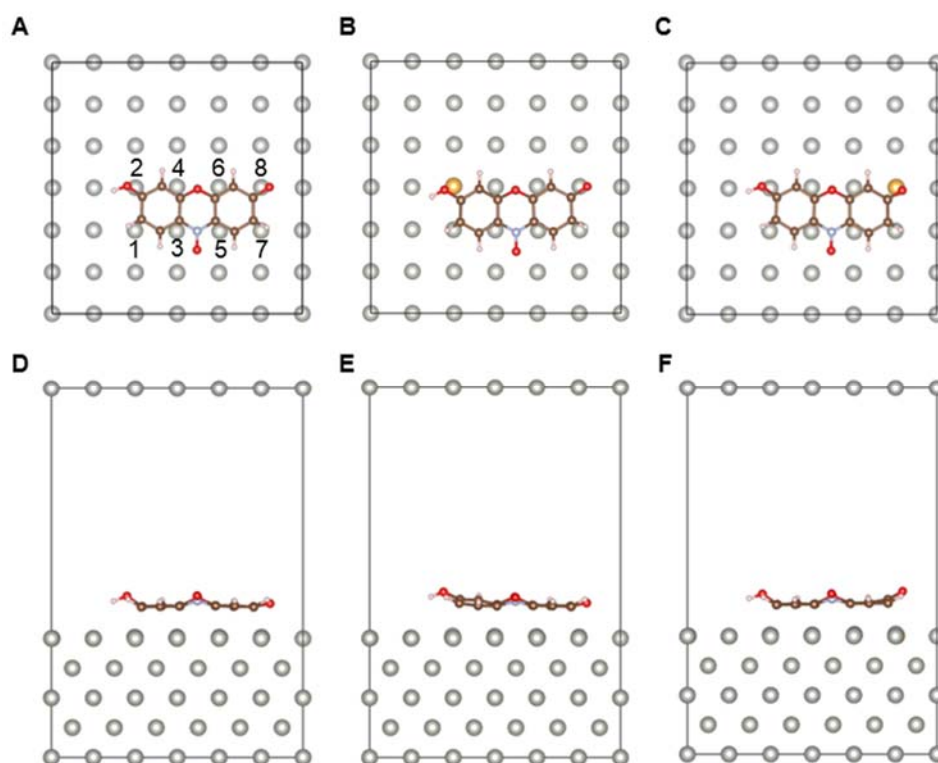

Figure S20. Adsorption geometries of resazurin on Au@Pd(100). (**A**) The most stable adsorption geometry of resazurin on Pd (100). Same as Structure III in Figure S18. The Pd atoms (labelled 1-8), which directly interact with resazurin, were individually replaced to build bimetallic surfaces. (**B**, **C**) The adsorption geometries of resazurin on Au@Pd(100) with substitutions at Pd atom no.2 and no.8, respectively, which are the two most stable adsorption geometries of all eight candidates formed by single-atom-substitutions. (**D-F**). Front views of structures in A-C, respectively.

Table S2. Geometric and charge properties of resazurin adsorbed on Pd(100) and single-atom substituted Au@Pd(100) bimetallic surfaces from DFT calculations

Rz-adsorption surface [a]	E_{ads} (eV)	Δr_{N-O} (Å) [b]	r_{M-O} (Å) [c]	r_{M-N} (Å) [c]	ΔQ_{Rz} (e) [d]	ΔQ_{N-O} (e) [d]
1	−3.464	0.007	3.436	2.815	0.499	0.053
2	−3.530	0.011	3.291	2.785	0.456	0.025
3	−3.416	0.009	3.479	2.924	0.490	0.115
4	−3.395	0.008	3.323	2.810	0.478	0.082
5	−3.409	0.009	3.503	2.949	0.487	0.088
6	−3.449	0.007	3.359	2.828	0.481	0.033
7	−3.511	0.004	3.446	2.814	0.473	−0.003
8	−3.536	0.004	3.396	2.796	0.447	−0.015
Pd(100)	−3.991	0.007	3.391	2.804	0.548	0.026

[a] The numbers refer to the single-atom-substitution position, as shown in Figure S20A. (2 and 8, highlighted in red, are the most stable ones.) [b] Δr_{N-O} is the elongation of the N–O bond compared to that of free resazurin (1.273 Å). [c] r_{M-O} (or r_{M-N}) refers to the average distance between O (or N) and all bridged metal atoms. [d] ΔQ_{Rz} and ΔQ_{N-O} refer to the net charge transfer from metal to resazurin and to the N–O fragment, respectively. All charges were calculated by Bader's analysis. For free resazurin, the total charge Q_{Rz} is 84 and the charge of the N–O fragment Q_{N-O} is 13.150.

6.3.2 Resazurin on Pd@Au(111) surface

Based on the most stable geometries of resazurin on Au(111) (Structure II in Figure S19), there are five surface Au atoms that dominate the interactions with resazurin (labelled 1-5 in Figure S21A). Similarly, for each of them, we substituted it with a Pd atom to construct a Pd@Au(111) bimetallic surface and subsequently optimized the adsorption geometry (Table S3). All five candidates have longer N–O bond length than that on Au(111) and the most stable one (substitution of Au atom no. 4) is shown in Figure S21B and D.
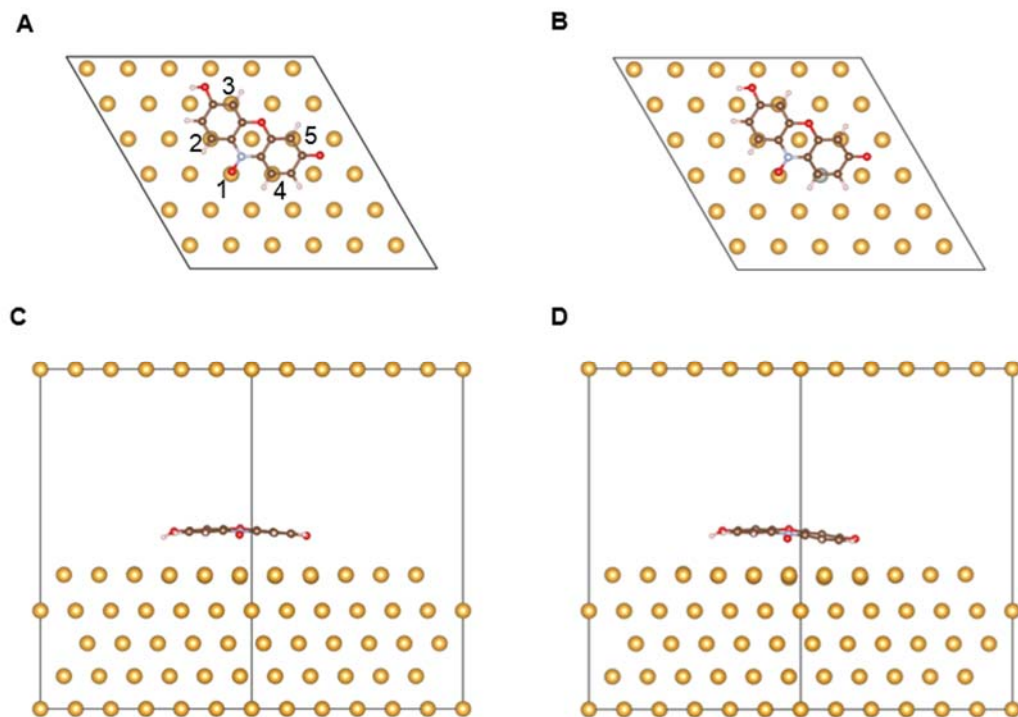
Figure S21. Adsorption geometries of resazurin on Pd@Au (111). (A) The most stable adsorption geometry of resazurin on Au(111); same as structure II in Figure S19. The Au atoms (labelled 1-5), which directly interact with resazurin, were individually replaced to build bimetallic surfaces. **(B)** The adsorption geometries of resazurin on Pd@Au(111) with substitution at Au atom no.4, which is the most stable adsorption geometry of all five candidates formed by single-atom-substitutions. **(C-D)** Rotated front views (in which the N–O of resazurin are pointing out of plane) of A and B.

Table S3. Geometric and charge properties of resazurin adsorbed on Au(111) and single-atom substituted Pd@Au(111) bimetallic surfaces from DFT calculations

Rz-adsorption surface [a]	E_{ads} (eV)	Δr_{N-O} (Å) [b]	r_{M-O} (Å) [c]	r_{M-N} (Å) [c]	ΔQ_{Rz} (e) [d]	ΔQ_{N-O} (e) [d]
1	−1.998	0.018	2.522	3.307	0.021	0.055
2	−2.021	0.010	2.702	3.351	0.006	0.038
3	−1.980	0.008	2.782	3.411	−0.010	0.096
4	−2.089	0.013	2.665	3.342	0.023	0.045
5	−2.024	0.007	2.826	3.424	0.002	0.090
Au(111)	−1.943	0.006	2.845	3.457	−0.025	0.016

[a] The numbers refer to the single-atom-substitution position, as shown in Figure S21A. (4, highlighted in red, is the most stable one.) [b] Δr_{N-O} is the elongation of the N–O bond compared to that of free resazurin (1.273 Å). [c] r_{M-O} refers to the distance between O and closest metal atom and r_{M-N} refers to the average distance between N and two bridged metal atoms. [d] ΔQ_{Rz} and ΔQ_{N-O} refer to the net charge transfer from metal to resazurin and to the N–O fragment, respectively. All charges were calculated by Bader's analysis. For free resazurin, the total charge Q_{Rz} is 84 and the charge of the N–O fragment Q_{N-O} is 13.150.

6.4 Charge transfer between the metal and the adsorbed resazurin

We evaluated the charge transfer between resazurin and metal surfaces (Table S2, Table **S3**). For resazurin on Pd(100), the overall net charge transfer is from Pd to resazurin (0.548 e) with a small portion of it to N–O (0.026 e), because the phenoxazine ring dominates the overall interaction (Figure S20A, D). In contrast, for resazurin on Au(111), the overall net charge transfer is from resazurin to Au ($-0.025e$, the minus sign refers to the resazurin-to-Au charge transfer direction), but the N–O fragment still gains charge (0.016 e) from the surface. We think the differences in charge transfer on Pd(100) and Au(111) surfaces might be related to the observed higher activity of Pd than Au (main text Figure 3A). On Pd(100), due to the fact that π^{*}_{NO} orbital, the charge accepter orbital in the back-donation interaction, is delocalized over the entire molecule (see main text Figure 5F), the charge transfer from Pd to ring structure could also go to N–O and contributes to the bond cleavage

On both Pd(100) and Au(111) surfaces, the net charge transfer between the metal and the N–O fragment is that the N–O fragment acquires charge from the metal surfaces, which indicates the back-donation (which results in a charge transfer into the N−O) is the more dominant interaction than forward-donation (which results in a charge transfer out of the N−O).

6.5 COHP analysis

In order to understand the adsorbate-surface bonding interactions, we did COHP analysis[23,24] and analyzed the interactions between metal and the N–O fragment of resazurin on Pd(100) and Au(111) surfaces (Figure 5C, D in main text). Figure S22 below are the COHP analyses of resazurin on Au@Pd(100) (substitution at Pd atom no.2) and Pd@Au(111) (substitution at Au atom no.4) bimetallic surfaces, which are qualitatively similar to the ones on monometallic surfaces: both forward- and back-donation bonding interactions were identified ($\pi_{\text{N-O}} + d$ and $d + \pi^{*}_{\text{N-O}}$, respectively) between the metal and the N−O fragment. Compared with the monometallic surfaces, we found both forward- and back-donations were strengthened, as indicated by the larger integrated area under metal–O curve in the COHP diagram (Table S4). These results could rationalize, from the electronic structure perspective, the enhanced activation of the N–O bond for cleavage on the bimetallic surfaces because both forward- and back-donations result in the weakening of the N–O bond (see more discussions in Section S6.6).
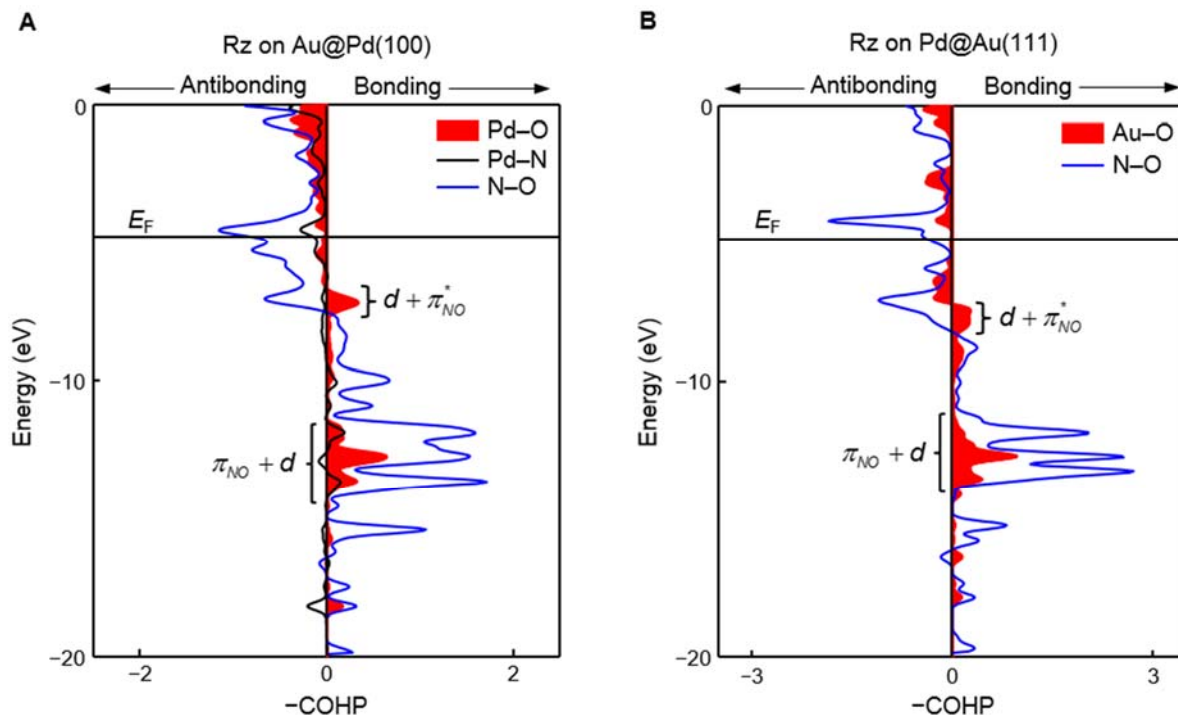
Figure S22. COHP analysis of resazurin on bimetallic surfaces. (A) The interactions between N−O and the bridged surface Pd atoms for resazurin on Au@Pd(100) (substitution at Pd atom no.2) surface, shown in Figure S20B and E. **(B)** The interactions between N−O and the closest surface Au atom for resazurin on Pd@Au(111) surface (substitution at Au atom no.4), shown in Figure S21B and D.

Table S4. Forward- and back-donations of metal–O interaction on monometallic and bimetallic surfaces [a]

Rz-adsorption surface	Forward-donation ($\pi_{N-O} + d$)	Back-donation ($d + \pi^*_{N-O}$)
Pd(100)	0.563	0.118
Au@Pd(100) [b]	0.645	0.166
Au(111)	0.657	0.121
Pd@Au(111) [c]	0.883	0.227

[a] The interactions are quantified by the integrated area under the metal-O curve in COHP analysis. [b] It refers to the Au@Pd(100) (substitution at Pd atom no.2, as shown in Figure S20B and E). [c] It refers to the Pd@Au(111) (substitution at Au atom no.4, as shown in Figure S21B and D).

6.6 MO diagram of resazurin

We analyzed the molecular orbitals (MOs) of resazurin in order to identify the MOs that participate in the adsorbate-surface interactions, specifically the forward- and back-donations. Based on the COHP analysis (Figure S22) and DOS of resazurin (Figure S23A), we focus on two energy ranges (−7 to −2 eV and −13 to −10 eV, highlighted in the brackets in Figure S23A), which are relevant to the forward- and back-donations. The MO diagram of resazurin (from Gaussian calculations) is qualitatively similar to its DOS diagram (from VASP), as shown in Figure S23B and C, which helps identify the MOs involved in the forward and back-donations.

For the back-donation interaction, which requires an unoccupied MO of resazurin that is antibonding in nature between N and O (Figure S22A, blue curve), the LUMO ($43\pi^*$ in Figure S23B) is a likely candidate to accept electron density from the metal d-block. Since this LUMO of resazurin is an anti-bonding orbital of the N−O fragment (Figure S24), donating electron density to this LUMO would weaken the N−O bond, thus activating it for cleavage. For the forward-donation interaction, there are a number of doubly occupied MOs in the corresponding energy range (Figure S23C). Since the resazurin molecule lies flat on the surface, the N−O orbitals should have lobes pointing toward the metal surface and perpendicular to the ring structure in order to form good orbital overlaps with the metal orbitals. Furthermore, the involved orbital of resazurin should be bonding in nature between the N and O atoms as shown by the COHP analysis in Figure S22A (blue curve). The π orbitals of N−O (20π and 25π, Figure S25) are thus likely candidates. We cannot differentiate these two, and simply picked 25π as a representative orbital for forward-donation interaction just to illustrate in Figure 5E in main text, as 25π is higher in energy and closer to the Fermi level as a frontier orbital.

Note: We matched the Fermi level of resazurin, calculated by VASP, with the midpoint between its LUMO and HOMO, calculated by Gaussian, to align DOS and MO diagrams (Figure S23B and C).
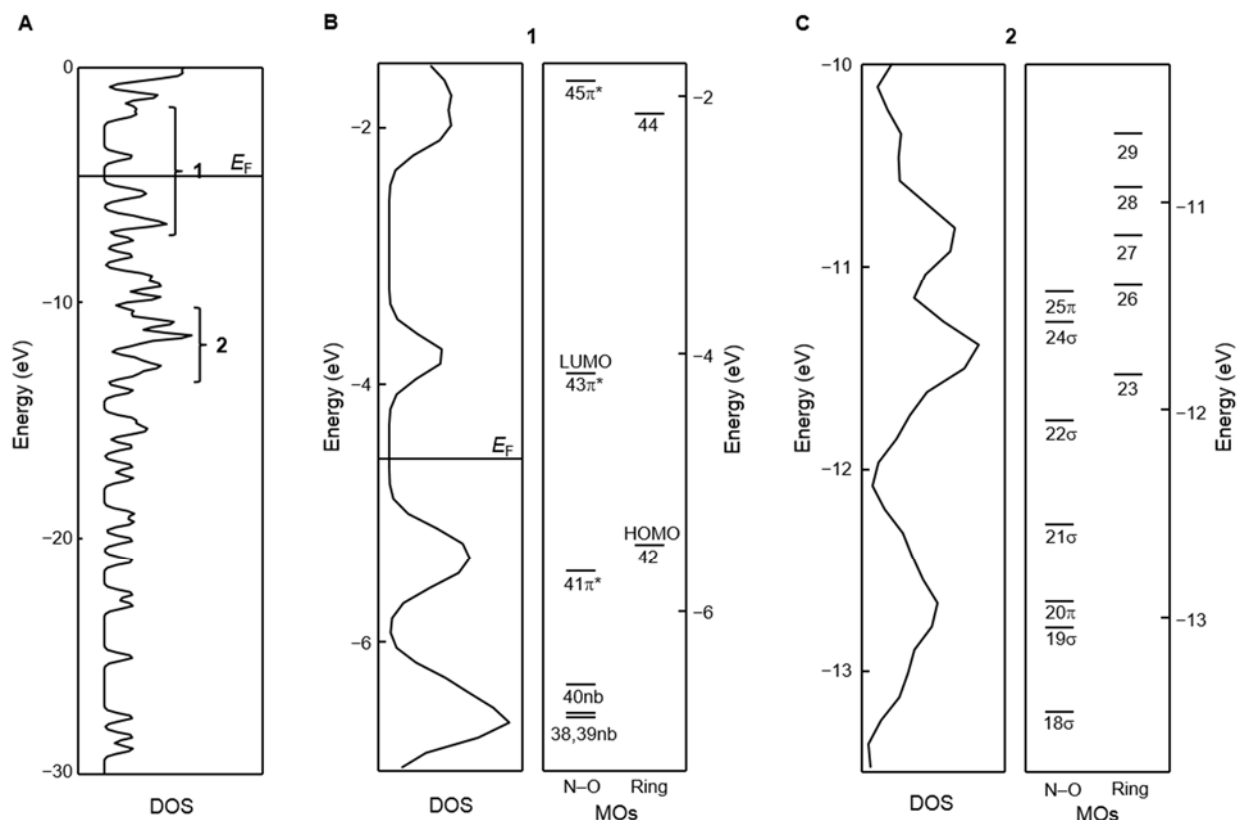

Figure S23. Resazurin bonding analysis. (**A**) DOS of resazurin from VASP calculations. The states in energy range 1 and range 2 (highlighted by brackets) are the relevant ones forming bonding interactions with metal surface. (**B**) MO analysis of resazurin in energy range 1: the left panel is the DOS from VASP and the right panel is the MO diagram of resazurin in the same energy range from Gaussian. The MOs are divided into two groups: the left and right columns represent ones with and without significant N–O fragment contributions, respectively. The MOs are labeled by the orbital number and the N–O bonding nature (if any), such as σ, π, and nb (non-bonding). (**C**) Same as B but for energy range 2. All the MOs in range 1 and range 2 are shown in Figure S24 and Figure S25, respectively.
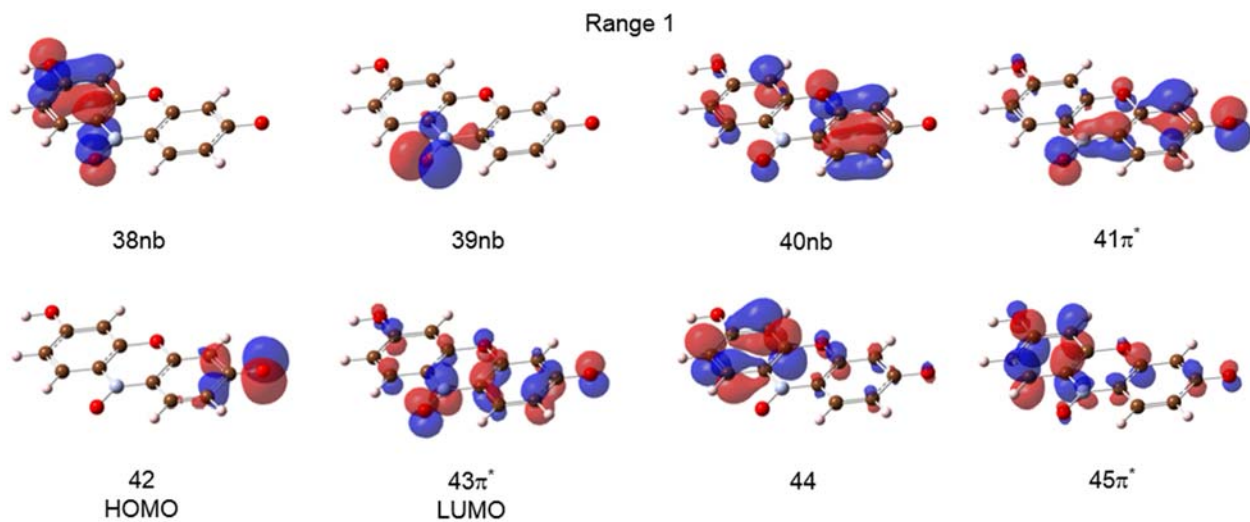
38nb 39nb 40nb 41π*

42
HOMO

43π*
LUMO

44

45π*

Figure S24. MOs of resazurin in energy range 1.

Range 2

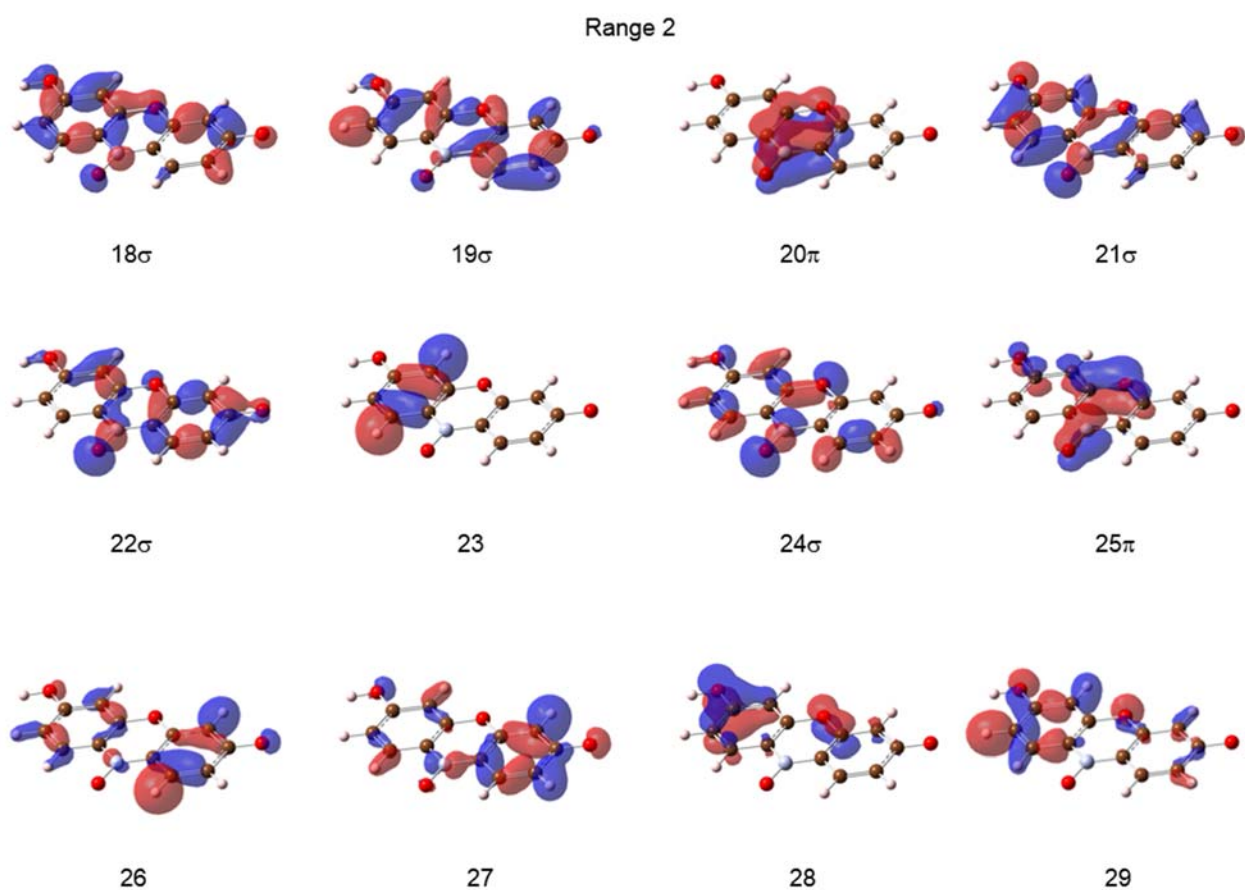18σ 19σ 20π 21σ

22σ 23 24σ 25π

26 27 28 29

Figure S25. MOs of resazurin in energy range 2.

6.7 DOS decomposition in correlation with the COHP analysis

To gain more information on the nature of orbitals involved in the forward- and back-donation interactions that were identified by COHP analysis, we examined the orbital compositions of relevant states. Since the COHP analyses of resazurin on monometallic and bimetallic surfaces gave qualitatively similar results, we use the monometallic cases to illustrate the decomposition of the DOS (Figure S26). Parallel to the COHP analysis (middle panels in Figure S26A and B), we show the decomposition of DOS into those of the involved metal atoms (left) and that of the N–O fragment (right). In the energy range corresponding to the forward-donation interaction (i.e., $\pi_{N-O} + d$, about −12 to −13 eV), the DOS is well below the d-block of Pd or and Au (about −7 to −8 eV) and has significant contributions from the N–O fragment (and little from the metal). Therefore, the energy levels for the forward-donation interactions comprise mainly of N-O fragment in character and are denoted as $\pi_{N-O} + d$. In the energy range corresponding to the back-donation interactions (i.e., $d + \pi^*_{N-O}$, about −7 to −8 eV), the DOS is in the d-block range and well below the LUMO of resazurin (about −4 eV); therefore, the energy levels for the back-donation interactions are mainly metal d in character and denoted as $d + \pi^*_{N-O}$. Note: in the DOS from the N–O fragment, there is a peak in the back-donation energy range (about −7 eV), which are due to the lone pairs of the O atom (corresponding to the orbitals 38, 39, 40 in Figure S24) and not relevant to the back-donation interactions.
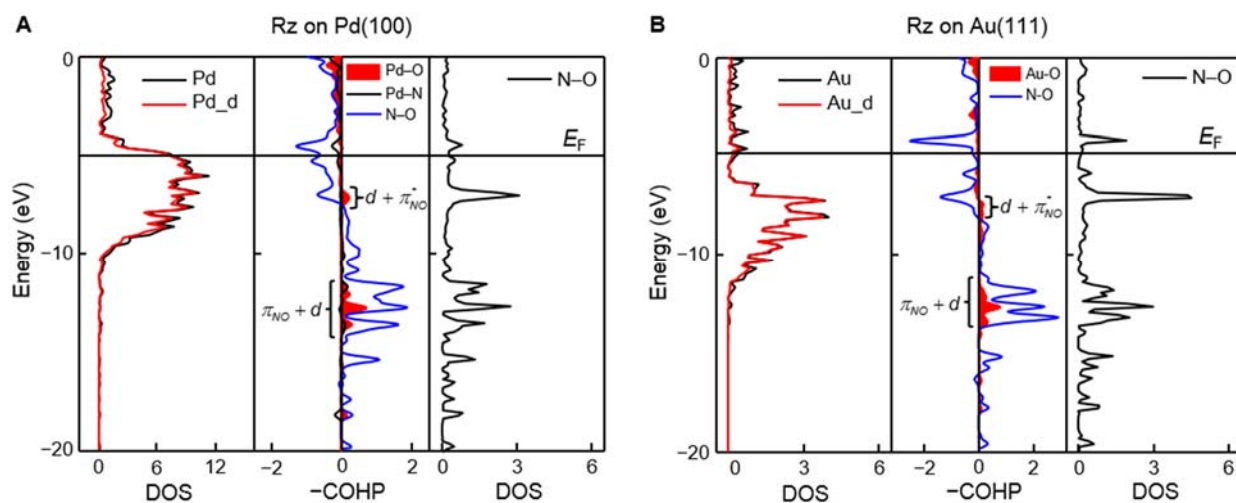

Figure S26. DOS decompositions of Rz adsorption on Pd(100) (A) and Au(111) (B) in correlation with the COHP analysis. (**A**) Resazurin on Pd(100). The middle panel is the COHP analysis of the interaction between the bridged Pd atoms and the N–O fragment of resazurin, which is also shown in Figure 5C in the main text. The left and right panels are the corresponding DOS from the four bridged Pd atoms (black lines; their d-orbital component is shown in red line) and N–O fragment of resazurin, respectively. (**B**) Same as A but for resazurin on Au(111). Here the DOS of Au is the Au atom right under the O of the N–O fragment. The COHP analysis (middle) is for the interaction between that Au atom and O, which is also shown in Figure 5D in the main text.

7. Additional references

(1)   Huang, X. Q.; Zheng, N. F. One-Pot, High-Yield Synthesis of 5-Fold Twinned Pd Nanowires and Nanorods. *J Am Chem Soc* **2009**, *131*, 4602-4603.

(2)   Zhou, X. C.; Andoy, N. M.; Liu, G. K.; Choudhary, E.; Han, K. S.; Shen, H.; Chen, P. Quantitative super-resolution imaging uncovers reactivity patterns on single nanocatalysts. *Nat Nanotechnol* **2012,** *7*, 237-241.

(3)   Andoy, N. M.; Zhou, X. C.; Choudhary, E.; Shen, H.; Liu, G. K.; Chen, P. Single-Molecule Catalysis Mapping Quantifies Site-Specific Activity and Uncovers Radial Activity Gradient on Single 2D Nanocrystals. *J Am Chem Soc* **2013,** *135*, 1845-1852.

(4)   Botella, P.; Corma, A.; Navarro, M. T. Single gold nanoparticles encapsulated in monodispersed regular spheres of mesostructured silica produced by pseudomorphic transformation. *Chem Mater* **2007,** *19*, 1979-1983.

(5)   Kundu, S.; Ravishankar, N. Rapid synthesis of hybrids and hollow PdO nanostructures by controlled in situ dissolution of a ZnO nanorod template: insights into the formation mechanism and thermal stability. *Nanoscale* **2016,** *8*, 1462-1469.

(6)   Zhou, X.; Xu, W.; Liu, G.; Panda, D.; Chen, P. Size-dependent catalytic activity and dynamics of gold nanoparticles at the single-molecule level. *J Am Chem Soc* **2010,** *132*, 138-146.

(7)   Jana, N. R.; Gearheart, L.; Murphy, C. J. Seed-mediated growth approach for shape-controlled synthesis of spheroidal and rod-like gold nanoparticles using a surfactant template. *Adv Mater* **2001,** *13*, 1389-1393.

(8)   Bueno, C.; Villegas, M. L.; Bertolotti, S. G.; Previtali, C. M.; Neumann, M. G.; Encinas, M. V. The excited-state interaction of resazurin and resorufin with amines in aqueous solutions. Photophysics and photochemical reaction. *Photochem Photobiol* **2002,** *76*, 385-390.

(9)   Balcerzyk, A.; Baldacchino, G. Implementation of laser induced fluorescence in a pulse radiolysis experiment - a new way to analyze resazurin-like reduction mechanisms. *Analyst* **2014,** *139*, 1707-1712.

(10)   Sambur, J. B.; Chen, T. Y.; Choudhary, E.; Chen, G. Q.; Nissen, E. J.; Thomas, E. M.; Zou, N. M.; Chen, P. Sub-particle reaction and photocurrent mapping to optimize catalyst-modified photoanodes. *Nature* **2016,** *530*, 77-80.

(11)   Chen, T. Y.; Santiago, A. G.; Jung, W.; Krzeminski, L.; Yang, F.; Martell, D. J.; Helmann, J. D.; Chen, P. Concentration- and chromosome-organization-dependent regulator unbinding from DNA for transcription regulation in living cells. *Nat Commun* **2015,** *6*, 7445.

(12)   Xu, W. L.; Shen, H.; Kim, Y. J.; Zhou, X. C.; Liu, G. K.; Park, J.; Chen, P. Single-Molecule Electrocatalysis by Single-Walled Carbon Nanotubes. *Nano Lett* **2009,** *9*, 3968-3973.

(13)   Kresse, G.; Furthmuller, J. Efficient iterative schemes for ab initio total-energy calculations using a plane-wave basis set. *Phys Rev B* **1996,** *54*, 11169-11186.

(14)   Kresse, G.; Furthmuller, J. Efficiency of ab-initio total energy calculations for metals and semiconductors using a plane-wave basis set. *Comp Mater Sci* **1996,** *6*, 15-50.

(15)   Perdew, J. P.; Burke, K.; Ernzerhof, M. Generalized gradient approximation made simple. *Phys Rev Lett* **1996,** *77*, 3865-3868.

(16)   Perdew, J. P.; Burke, K.; Ernzerhof, M. Generalized gradient approximation made simple (vol 77, pg 3865, 1996). *Phys Rev Lett* **1997,** *78*, 1396-1396.

(17)   Blochl, P. E. Projector Augmented-Wave Method. *Phys Rev B* **1994,** *50*, 17953-17979.

(18)   Kresse, G.; Joubert, D. From ultrasoft pseudopotentials to the projector augmented-wave method. *Phys Rev B* **1999,** *59*, 1758-1775.

(19) Grimme, S.; Antony, J.; Ehrlich, S.; Krieg, H. A consistent and accurate ab initio parametrization of density functional dispersion correction (DFT-D) for the 94 elements H-Pu. *J Chem Phys* **2010,** *132*, 154104.

(20) Hermann, K. *Crystallography and surface structure : an introduction for surface scientists and nanoscientists*; Wiley-VCH: Weinheim, Germany, 2011.

(21) Henkelman, G.; Arnaldsson, A.; Jonsson, H. A fast and robust algorithm for Bader decomposition of charge density. *Comp Mater Sci* **2006,** *36*, 354-360.

(22) Tang, W.; Sanville, E.; Henkelman, G. A grid-based Bader analysis algorithm without lattice bias. *J Phys-Condens Mat* **2009,** *21*, 084204.

(23) Deringer, V. L.; Tchougreeff, A. L.; Dronskowski, R. Crystal Orbital Hamilton Population (COHP) Analysis As Projected from Plane-Wave Basis Sets. *J Phys Chem A* **2011,** *115*, 5461-5466.

(24) Dronskowski, R.; Blochl, P. E. Crystal Orbital Hamilton Populations (Cohp) - Energy-Resolved Visualization of Chemical Bonding in Solids Based on Density-Functional Calculations. *J Phys Chem-Us* **1993,** *97*, 8617-8624.

(25) Maintz, S.; Deringer, V. L.; Tchougreeff, A. L.; Dronskowski, R. LOBSTER: A Tool to Extract Chemical Bonding from Plane-Wave Based DFT. *J Comput Chem* **2016,** *37*, 1030-1035.